

Performance and Controlling Regimes Analysis of Methane Steam Reforming on Ru/-Al₂O₃ Cordierite Monoliths

Original

Performance and Controlling Regimes Analysis of Methane Steam Reforming on Ru/-Al₂O₃ Cordierite Monoliths / Moncada Quintero, C. W.; Babar, R. Z.; Specchia, S. - In: Sustainable Development for Energy, Power, and Propulsion / De A., Gupta A.K., Aggarwal S., Kushari A., Runchal A.K.. - STAMPA. - Singapore : Springer Nature Singapore Pte Ltd., 2021. - ISBN 978-981-15-5667-8. - pp. 91-131 [10.1007/978-981-15-5667-8_5]

Availability:

This version is available at: 11583/2833394 since: 2020-10-03T17:41:34Z

Publisher:

Springer Nature Singapore Pte Ltd.

Published

DOI:10.1007/978-981-15-5667-8_5

Terms of use:

This article is made available under terms and conditions as specified in the corresponding bibliographic description in the repository

Publisher copyright

Springer postprint/Author's Accepted Manuscript (book chapters)

This is a post-peer-review, pre-copyedit version of a book chapter published in Sustainable Development for Energy, Power, and Propulsion. The final authenticated version is available online at: http://dx.doi.org/10.1007/978-981-15-5667-8_5

(Article begins on next page)

Performance and controlling regimes analysis of methane steam reforming on Ru/ γ -Al₂O₃ cordierite monoliths

Carmen W. Moncada Quintero (0000-0002-9058-3646), Roman Z. Babar, Stefania Specchia (0000-0003-3882-3240) *

Affiliation

*Corresponding Author: Tel.: +39 011 0904608 Fax: +39 011 0904699

E-mail address: stefania.specchia@polito.it

Abstract

In the frame of methane steam reforming (MSR) process intensification for H₂ production, catalysts based on Ruthenium (Ru) supported on Alumina (Al₂O₃) on cordierite monolith have been studied in terms of catalytic performance, mass and heat transfer effects. Firstly, we compared the catalytic activity of Ru and Rh supported catalysts. Secondly, we study the effect of catalyst loading by varying the amount of carrier and active metal phase corresponding to 3.20, 6.45 and 12.89 mg cm⁻². Then, we evaluated the mass/heat transfer effects and controlling regimes for the best-selected catalyst. Finally, the best-selected catalyst was characterized by means of Brunauer-Emmet-Teller (BET), X-Ray diffraction analysis (XRD) and Field-emission scanning electron microscopy (FESEM). The experiments were carried out in the temperature range of 550 to 850 °C, steam to carbon molar ratio (S/C) of 3.0 and different weight hourly space velocity (WHSV= 750, 1500 and 3000 NI h⁻¹ g_{cat}⁻¹). The catalyst with 1.5% Ru on 10% Al (1.5Ru10Al) was found to be the most promising toward the MSR reaction in terms of CH₄ conversion and H₂ production.

This catalyst operates in a mixed regime for all temperature range studied, in which both the kinetic and the intraparticle diffusion co-exist. For the 1.5Ru10Al catalyst, the external thermal effects are important a temperature below 725°C, while that intraparticle heat effects are absent for all the range of temperature studied. An excellent stability of the 1.5Ru10Al catalyst was observed over 70 h of time on stream (TOS) for MSR process.

Keywords: mass transfer; heat transfer; hydrogen production; methane steam reforming

Nomenclature

Fluid properties

$C_{CH_4,in}; C_b$	Methane concentration in feed mixture (bulk) ($\text{mol}\cdot\text{m}^{-3}$)
C_{pf}	Heat capacity of the gas mixture ($\text{J mol}^{-1} \text{K}^{-1}$)
C_{pi}	Heat capacity of i component ($\text{J mol}^{-1} \text{K}^{-1}$)
C_s	Methane concentration at catalyst surface ($\text{mol}\cdot\text{m}^{-3}$)
D_{CH_4-mix}	Diffusivity of CH_4 in gas phase ($\text{m}^2\cdot\text{s}^{-1}$)
$D_{CH_4,e}$	Effective diffusivity of CH_4 in coated layer ($\text{m}^2\cdot\text{s}^{-1}$)
D_{CH_4-i}	Binary diffusion of CH_4 and i gas species ($\text{m}^2\cdot\text{s}^{-1}$)
D_k	Knudsen diffusion ($\text{m}^2\cdot\text{s}^{-1}$)
h_e	Heat transfer coefficient of gas mixture ($\text{W m}^{-2} \text{K}^{-1}$)
$k_{m,e}, k_G$	Mass transfer coefficient of CH_4 ($\text{m}\cdot\text{s}^{-1}$)
$k_{m,app}$	Apparent mass transfer coefficient ($\text{m}\cdot\text{s}^{-1}$)
M_{CH_4}	Molecular weight of CH_4 ($\text{kg}\cdot\text{kmol}^{-1}$)
M_i	Molecular weight of i compound ($\text{kg}\cdot\text{kmol}^{-1}$)
M_{mix}	Molecular weight of gas mixture ($\text{kg}\cdot\text{kmol}^{-1}$)
P	Transverse Peclet number (m)
R_g	Universal gas constant ($\text{J}\cdot\text{mol}^{-1}\cdot\text{K}^{-1}$)
u_o	Inlet gas velocity ($\text{m}\cdot\text{s}^{-1}$)
v_{CH_4}	Molar volume of CH_4 ($\text{cm}^3\cdot\text{mol}^{-1}$)
v_i	Molar volume of i compound ($\text{cm}^3\cdot\text{mol}^{-1}$)
y_{CH_4}	Mole fraction of CH_4
y_i	Viscosity of i compound ($\text{kg}\cdot\text{m}^{-1}\cdot\text{s}^{-1}$)
μ_i	Viscosity of i compound ($\text{kg}\cdot\text{m}^{-1}\cdot\text{s}^{-1}$)
μ_f	Viscosity of gas mixture ($\text{kg}\cdot\text{m}^{-1}\cdot\text{s}^{-1}$)
λ_i	Thermal conductivity of i component ($\text{W m}^{-1} \text{K}^{-1}$)

λ_{mix}	Thermal conductivity of gas mixture ($\text{W m}^{-1} \text{K}^{-1}$)
ρ_f	Density of gas mixture (kg m^{-3})

Reaction data

F_{tot}	Total gas flow rate ($\text{m}^3 \cdot \text{s}^{-1}$)
k_{obs}	Observed 1 st order reaction rate constant (s^{-1})
k_s	Surface reaction rate constant
P	Reaction pressure (kPa)
r_{CH_4}	Reaction rate for CH_4 ($\text{kmol} \cdot \text{kg}^{-1} \cdot \text{s}^{-1}$)
R_{CH_4}	Volumetric reaction rate for CH_4 ($\text{kmol} \cdot \text{m}^{-3} \cdot \text{s}^{-1}$)
T	Reaction temperature (K)
T_b, T_s	Temperature in the bulk of the gas phase and surface of the catalyst layer (K)
$T_{b,c}$	Temperature in the bulk of the catalyst layer (K)
ϕ	Thiele modulus
H	Effectiveness factor
ΔH_r	Heat of MSR reaction (J mol^{-1})
λ_{cat}	Catalyst thermal conductivity ($\text{W m}^{-1} \text{K}^{-1}$)
λ_e	Effective thermal conductivity ($\text{W m}^{-1} \text{K}^{-1}$)

Monolith properties

A_{ch}	Area of a single bare channel (m^2)
A_m	Monolith area (m^2)
A_{Ω_e}	Cross-sectional area of fluid phase (m^2)
A_{Ω_i}	Cross-sectional area of catalyst layer (m^2)
d_h	Hydraulic diameter (m)
d_f	Average channel dimension (m)
D	Inner length of the channel (m)
D_m	Monolith diameter (m)
GSA	Geometric surface area ($\text{m}^2 \cdot \text{m}^{-3}$)
l_w	Channel width (m)
L_m	Monolith length and diameter (m)
n	Cell density ($\text{N}^\circ \text{ cell} \cdot \text{m}^{-2}$)
P_c	Interfacial perimeter (m)
R_{Ω_e}	Characteristic length for gas phase (m)
R_{Ω_i}	Characteristic length for coated layer (m)
ε	Voidage of square channel
δ_w	Wall thickness (m)
ζ	Cell density (cpsi)

Coated layer properties

$k_{m,l}$	Internal mass transfer coefficient (m)
-----------	--

r_p	Pore radius (m)
S_{BET}	Specific surface area ($\text{m}^2 \text{g}^{-1}$)
V_{BJH}	Total pore volume ($\text{cm}^3 \text{g}^{-1}$)
δ_c	Coated layer thickness (m)
ε_c	Coated layer porosity
ρ_c	Coated layer density ($\text{kg} \cdot \text{m}^{-3}$)
τ_c	Tortuosity factor

Resistances

R_e	External mass transfer resistance (s m^{-1})
R_i	Internal mass transfer resistance (s m^{-1})
R_r	Reaction resistance (s m^{-1})
R_t	Overall resistance (s m^{-1})

Characteristic times

t_c	Characteristic contact time (s)
t_d^e	Transverse diffusion time for the flow area (s)
t_d^i	Transverse diffusion time for the coated area (s)
t_r	Characteristic reaction time (s)
t_z	Longitudinal diffusion time (s)

Dimensionless numbers

A	$D_{\text{CH4-mix}}/D_{\text{CH4,e}}$ ratio
B	R_{Qi}/R_{Qe} ratio
Ca	Carberry number
Le	Lewis number
Pr	Prandtl number
Re	Reynold number
Sc	Schmidt number
Sh_i, Sh_e	Internal/external Sherwood number
$Sh_{i\infty}, Sh_{e\infty}$	Asymptotic internal/external Sherwood number
Sh_{app}	Apparent Sherwood number
β_{in}, β_{ext}	Dimensionless internal/external Prater number
γ_b, γ_s	Arrhenius number at the bulk and surface of the gas phase
χ	Damkholer for interphase heat transport
ψ	Damkholer for intraparticle heat
x	Radial coordinate

Abbreviations

BET	Brunauer-Emmet-Teller
-----	-----------------------

EDX	energy dispersive X-ray
FESEM	field emission scanning electron microscopy
ID	internal diameter
MSR	methane steam reforming
NDIR	near D infra red
S _{BET}	specific surface area calculated by BET method
SCS	solution combustion synthesis
S/C	steam to carbon ration
TOS	time on stream
WGS	water gas shift
WHSV	weight hourly space velocity
XRD	X-ray diffraction

1. INTRODUCTION

Hydrogen (H₂) is one of the most abundant elements in the Earth's crust and due to its capability to drive the generation of electricity without emitting harmful pollutants, H₂ is considered as a prominent clean, environmentally benign and safe-to-handle major energy carrier of the future [1, 2]. Nowadays, H₂ is used in several industrial processes such as refining, treating metals, and food processing. In addition, H₂ is an essential building block for the production of ammonia, and thus fertilizers, and of methanol, utilized as a part of the production of many polymers [3–7]. The most important source of H₂ today is natural gas (~97 % of CH₄) with approximately 80% efficiency. In fact, more than 90% of the world's H₂ is produced by steam reforming (SR), being the most viable option for supporting a future hydrogen economy [8, 9]. Methane steam reforming (MSR) is a highly endothermic reaction (Reaction 1) accompanied mainly by the side reaction of the water gas shift (WGS), which is slightly exothermic (Reaction 2):



To be feasible at relatively low pressure and temperature ($T < 1000 \text{ }^\circ\text{C}$, $P < 5 \text{ bars}$), these reactions are carried out in the presence of a catalyst. Nickel-based catalysts are actually the most widely used for industrial reforming processes because of their high availability and low cost [8–10]. However, the catalytic activity gradually decreases because of carbon deposition and sintering of Ni. Catalyst systems based on noble metals have been extensively studied by many researchers, giving rise to excellent catalytic performances towards MSR processes [11, 12]. Noble metals such as Ru, Rh, Pd, Pt, and Ir have a higher barrier for carbon formation during operation than Ni. Particularly, whiskers carbon formation (caused by carbon deposition) can be problematic at severe condition for an effective performance of the catalyst [13]. Moreover, the catalyst may eventually break down [14]. Among

the noble metals, Ru and Rh are the most active metals with comparable performance, while Ru is the most promising candidate due to its lower price [11–15]. On the other hand, the nature of the support in MSR may also have a significant impact on the catalytic activity. Carrier materials for MRS catalysts require high specific surface area, wider pore structure easily accessible for gaseous transport, and thermal stability at high temperature ($< 1000\text{ }^{\circ}\text{C}$), even in the presence of steam [16]. Alumina (Al_2O_3) is widely used as catalyst carrier because it is inexpensive, reasonably thermally stable and can provide a wide range of specific surface area and porosity through its different phases [17, 18]. Ferreira-Aparicio et al. [19] investigated the role of Al_2O_3 support on the catalytic activity of Ru catalysts during MSR. They found that surface hydroxyl groups play a main role in the catalyst's resistance to deactivation. In the same way, Berman et al. [20] reported that during 10 days of operation of 1 wt.% Ru/ $\gamma\text{-Al}_2\text{O}_3$ catalyst in the temperature range of 600–900 $^{\circ}\text{C}$, the activity was stable without carbon depositions and change of mechanical properties of the catalyst.

Nowadays, research on MSR reaction is mainly devoted to improve the catalyst performance by producing as much H_2 as possible. Recently, the attention is focused on structured systems with active components supported on different configurations such as monoliths, foams, and honeycombs [16, 21–24]. In particular, monolith catalysts have been widely used in many applications due to for their excellent mechanical and chemical durability, high geometric surface area, rapid response to transient operation, low pressure drop and smaller sizes than reactors with traditional catalyst pellet materials. Furthermore, monolith reactors offer other advantages such as reduced capital cost, smaller footprints, and potentially easier transportation compared to fixed-bed reactors [25–27].

Several studies have shown that structured catalysts improve heat and mass transfer mechanisms between the fluid and solid phases. Especially, for endothermic process, high thermal conductive supports allow optimal thermal management in the catalytic volume maximizing heat transfer from the heating medium to the catalytic volume and reducing the temperature gradient due to the endothermicity of the reaction [28]. According to Tronconi et al. [28, 29], the effective thermal conductivity of a structured catalysts depends fundamentally on the conductivity of the substrate and that of the solid carrier deposited on the substrate. On the other hand, it is well known that in many heterogeneous catalytic reactions, the overall rate of reaction is often limited by mass transfer processes, which include both the internal diffusion (at intermediate temperatures) and external diffusion (at sufficiently high temperatures) of components into and out of the catalyst, especially for highly exothermic or endothermic reactions such as combustion or steam reforming [23, 24, 30, 31].

In the present work, we investigated the catalytic performance towards MSR of Ru and Rh on $\gamma\text{-Al}_2\text{O}_3$ catalysts supported on ceramic cordierite monoliths of square channel. Firstly, we compared the catalytic performance in terms of CH_4 conversion, H_2 production, CO selectivity and H_2/CO molar ratio of Rh and Ru supported on $\gamma\text{-Al}_2\text{O}_3$. Secondly, we study the influence of the catalyst loading by varying the amount of carrier and active metal phase. Then, we evaluated the different controlling regimes (kinetic, intraparticle, or interphase diffusion control)

and heat transfer effects for the best catalyst. All cordierite monoliths were coated by solution combustion synthesis. Finally, we evaluated the stability of the catalyst on the best-selected one.

2. METHODS

2.1. Chemicals and monoliths

Aluminium (III) nitrate nonahydrate, $\text{Al}(\text{NO}_3)_3 \cdot 9\text{H}_2\text{O}$ ($\geq 98\%$ purity), ruthenium (III) nitrosyl nitrate, $6\text{Ru}(\text{NO})(\text{NO}_3)_3$ ($\geq 98\%$ purity), rhodium(III) chloride, RuCl_3 ($\geq 98\%$ purity), urea, $\text{CH}_4\text{N}_2\text{O}$ ($\geq 99\%$ purity) were purchased from Sigma–Aldrich. All aqueous solutions were prepared using ultrapure water (Millipore Milli-Q system with resistivity $> 18 \text{ M}\Omega \text{ cm}$). For catalytic activity tests, pure CH_4 , H_2 , and N_2 gasses (purity 99.999%) were supplied in cylinders provided by SIAD S.p.A. (Italy) and used as received.

Ceramic monoliths of square channel (100 cell per in^2) made of cordierite in dimensions of 40 mm diameter by 30 mm were provided by Chauger Honeycomb Ceramics Co. (Taiwan).

2.2. Catalysts preparation

Before the catalyst deposition, cordierite monoliths were cleaned in an ultrasonic bath with a water/acetone solution (50/50 vol.%) for 30 min and dried at 120°C for 2 h. The catalytic layer based on Ru supported on $\gamma\text{-Al}_2\text{O}_3$ was coated by *in-situ* solution combustion synthesis (SCS) following the detailed procedure discussed in our previous work [32]. Briefly, the necessary amounts of aluminum nitrate, ruthenium nitrosyl nitrate as precursors and urea as fuel were dissolved in aqueous solution (3 M) under vigorous stirring. The ratio between the amount of urea used and the stoichiometric amount (Φ) was equal to 1 [33, 34]. Then, each monoliths was dipped in the aqueous solution for 2-3 min and then introduced into a muffle furnace preheated at 600°C for 10 min, where the combustion reaction occurred, letting the formation of the catalytic layer, and rapidly cooled down to room temperature in few minutes. The operation was repeated until the design weight of $\text{Ru}/\gamma\text{-Al}_2\text{O}_3$ was reached. Finally, the coated monoliths were calcined at 600°C for 2 h in static air.

For comparison of the catalytic performance, Rh-based catalysts were also prepared with the same procedure by using the corresponding nitrate of the active metal. A set of X wt.% ($X = 1.5$ and 3) of metal active phase (Ru, Rh) supported on $\gamma\text{-Al}_2\text{O}_3$ (with varying carrier loadings equal to 5, 10 and 20 wt.% compared to the weight of the monolith) were prepared, according to Table 1.

Metal	Carrier	Catalyst	Abbreviation
1.5% Ru	5% Al ₂ O ₃	1.5% Ru / 5% Al ₂ O ₃	1.5Ru5Al
3.0% Ru	5% Al ₂ O ₃	3.0% Ru / 5% Al ₂ O ₃	3Ru5Al
1.5% Ru	10% Al ₂ O ₃	1.5% Ru / 10% Al ₂ O ₃	1.5Ru10Al
1.5% Ru	20% Al ₂ O ₃	1.5% Ru / 20% Al ₂ O ₃	1.5Ru20Al
1.5% Rh	10% Al ₂ O ₃	1.5% Ru / 10% Al ₂ O ₃	1.5Rh10Al

Table 1. List of catalyst prepared by varying metal and carrier load.

2.3. Catalytic tests

The catalytic activity of coated monoliths was evaluated towards MSR in a tubular reactor of AISI 310 (40 mm ID) placed in an electric oven, which provided sufficient heat to vaporize water. The entire plant was set to provide 3 kW of energy. The micro-reactor temperatures were measured by two K-type thermocouples located, respectively, at the inlet and outlet of the coated monolith. Before starting catalytic tests, the structured catalysts were reduced *in situ* sending a flow of 100 Nml min⁻¹ of H₂ at 200 °C for 1 h. The catalytic tests were performed over a temperature range of 550-850 °C, at different steam-to-carbon molar ratios (S/C: 3-3.2) and weight hourly space velocities (WHSV 750-3000 Nl h⁻¹ g_{cat}⁻¹). Mass flow controllers (Brooks Instrument Smart Mass Flow) were used to measure and control the flow of gaseous reactants. The gas stream composition at the reactor outlet is monitored by an ABB gas analyzer (NDIR module Uras 14 for CO/CO₂/CH₄, paramagnetic module Magnos 106 for O₂ and H₂; water removed prior to entering the analyzer in a condenser at 3 °C). For all catalytic tests, measurements were repeated at least three times to assure their reproducibility and to check any possible aging phenomena on the structured catalysts.

The investigated catalysts were compared on the basis of CH₄ conversion, H₂ production, CO selectivity and H₂/CO molar ratio. The CH₄ conversion is calculated to determine the amount of inlet CH₄ that has reacted and converted to products (Equation 3). This value is based on the total dry outlet flow rate (F_{out,dry}), the inlet CH₄ flow rate (CH_{4,inlet}) and the CH₄ concentration in the product mixture (CH_{4,conc}).

$$CH_4 \text{ conversion} = \left[1 - \frac{\left(\frac{CH_{4,conc} \times F_{out,dry}}{100} \right)}{CH_{4,inlet}} \right] \times 100 \quad (3)$$

The H₂ production is the H₂ concentration in the product mixture (H_{2,conc}). The H₂ selectivity (Equation 4) is based on the molar volume of gas mixture (assuming it is an ideal gas mixture) and the CH₄ and H₂ outlet flowrates (CH_{4,outlet} and H_{2,outlet}, respectively).

$$H_2 \text{ Selectivity} = \left[\frac{H_{2outlet}}{\left(\left(\frac{CH_{4inlet}}{Molecular \ Volume} \right) - CH_{4outlet} \right)} \right] \times 100 \quad (4)$$

The CO selectivity (**Errore. L'origine riferimento non è stata trovata.**) is based on the molar volume of gas mixture (assuming it is an ideal gas mixture) and the CH₄ and CO outlet flowrates (CH_{4, outlet} and CO_{outlet}, respectively).

$$CO \text{ Selectivity} = \left[\frac{CO_{outlet}}{\left(\left(\frac{CH_{4inlet}}{Molecular \ Volume} \right) - CH_{4outlet} \right)} \right] \times 100 \quad (5)$$

Finally, the molar ratio of H₂/CO (Equation 6) is monitored to analyze the product in syngas concentration.

$$H_2/CO \text{ Ratio} = \frac{H_{2outlet}}{CO_{outlet}} \quad (6)$$

2.4. Characterization on the best-selected catalyst

The specific surface area, textural properties of powder and structured samples were determined by N₂ physisorption at −196 °C using an ASAP 2020 instrument from Micromeritics. Prior to analysis, about 100 mg of each sample was outgassed overnight at 150 °C under high vacuum. The specific surface areas (S_{BET}) were determined by Brunauer-Emmet-Teller (BET) method in the relative pressure range of 0.05 and 0.30.

By using the same apparatus, the chemisorption analysis was carried out, in order to evaluate the active metals dispersion on supports. H₂ saturation was first performed by flowing 20 Ncm³ min^{−1} of H₂ for 2 h at 350 °C, and at the end, a He flow rate of 20 Ncm³ min^{−1} for 1.5 h was fed to the apparatus increasing the temperature to 370 °C. Then, at room temperature, a mixture of 10% CO in He was injected in pulses of 500 NμL each, until the fulfillment of constant outlet peaks. The amount of adsorbed gas was determined as the difference between the total injected volume and the residual escaped one. The metal dispersion on the carrier surface was determined as follows:

$$D_{\%} = 100 \cdot S_f \cdot \frac{V_{ads} \cdot M_{me}}{V_g \cdot F_{me}} \quad (7)$$

considering the stoichiometric factor S_f is equal to 1 (i.e., each Ru atom adsorbed one CO molecule), the total volume of CO chemisorbed refers to the mass of the carrier used for the analysis in Ncm³ g^{−1} (V_{ads}), the metal atomic weight M_{me} (101.07

g mol⁻¹ for Ru) and the total mass fraction of the metal on the catalyst (expressed as g_{me} g⁻¹ of carrier), and that one gas g_{mole}, V_g , occupies 22,414 cm³ at normal conditions.

X-ray diffraction (XRD) patterns were collected using a Philips X-Pert MPD X-ray diffractometer equipped with Copper K α radiation at 40 kV and 30 mA to verify the effective composition of the samples and derive qualitative indications of the presence of comparatively large noble metals crystallite from its eventually visible peaks. All powder samples were scanned in the 2 θ range of 20-70° over 1h. The peaks were assigned according to the PCPFWIN database.

The surface morphology of the catalyst was examined by using Field-emission scanning electron microscopy FESEM (FESEM JEOL-JSM-6700F instrument). The elemental composition analysis was carried out by energy dispersive X-ray spectroscopy EDX (Oxford Instruments Inca EDX apparatus).

The geometrical properties of monoliths for square channel are calculated by [35–39]:

$$n = \frac{1}{(D+\delta_w)^2} \quad (8)$$

$$\varepsilon = D^2 \cdot n \quad (9)$$

$$GSA = \frac{4(\sqrt{\varepsilon}-\varepsilon)}{\delta_w} \quad (10)$$

$$d_h = \frac{4 \cdot \varepsilon}{GSA} \quad (11)$$

where n is the cell density (N° cell·m⁻²), D inner length of the channel (m), δ_w is the wall thickness (m), ε is the voidage for square channels, GSA is the geometric surface area (m² m⁻³) and d_h is the hydraulic diameter (m).

2.5. Stability measurements

Stability tests were performed over 70 h of time on stream (TOS) at 800 °C for the best-selected catalyst. The reactor was fed with a reactive mixture containing CH₄ and H₂O with a S/C equal to 3 and WHSV equal to 750 Nl h⁻¹ g_{cat}⁻¹. At 30 h of TOS the WHSV was increased up to 1500 Nl h⁻¹ g_{cat}⁻¹. At 50 h of TOS the WHSV was reported to 750 Nl h⁻¹ g_{cat}⁻¹ till the end of the experiment (70 h of TOS), according to the thermal cycling shown in Figure 1.

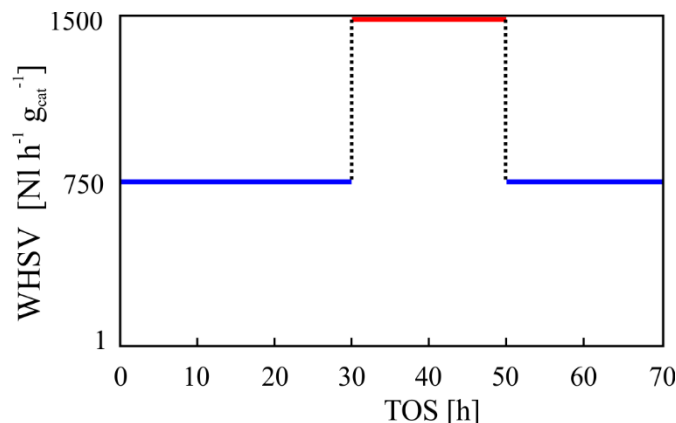


Fig. 1. Thermal cycling for stability tests: WHSV vs WHSV at 800 °C and S/C of 3.

3. RESULTS AND DISCUSSION

3.1. Ru/Rh metal on γ -Al₂O₃ carrier: metal-base catalysts comparison

In order to compare the catalytic performance of noble metals coated on monolith supports, Ru and Rh (active metal loading equal to 1.5 wt.%) on γ -Al₂O₃ (10 wt.% on the bare cordierite monolith) were tested toward the MSR reaction. The experiments were carried out in the temperature range of 550 to 850 °C, S/C equal to 3.0, and WHSV of 750 NI h⁻¹ g_{cat}⁻¹.

As can be seen from Figure 2.a., both noble-metal-based catalysts do not reach complete methane conversion. However, the catalytic activity of the Ru-based one was found to be the most promising toward the MSR reaction in terms of CH₄ conversion, H₂ production, and CO selectivity. At temperatures higher than 750 °C, CH₄ conversion for 1.5Ru10Al catalyst remained slightly stable at 88.2 %, reaching the maximum conversion (91.0 %) at 800 °C, while for 1.5Rh10Al catalyst, CH₄ conversion increased for the entire temperature range studied achieving the maximum value of 87 % at 850 °C. On the other hand, H₂ produced for both catalysts was nearly the same, except at temperatures between 600-700 °C, where H₂ production was slightly higher for 1.5Ru10Al catalyst (Fig.2.a). As far as the selectivity of CO is concerned, both catalysts showed an increase in CO selectivity at temperatures between 550-700 °C. At temperatures above 700 °C, CO selectivity for 1.5Rh10Al catalyst remained stable at approximately 42 %, while for 1.5Ru10Al catalyst it continued to increase up to 750 °C, where it reached the maximum selectivity value of 50.25 % and then decreased due probably to the WGS reaction, which converts CO into CO₂ (Fig. 2.b). In fact, as shown in Figure 2.c, at temperatures between 725-850 °C, the H₂/CO molar ratio was slightly higher for the Rh-based catalyst because of CO consumption (WGS reaction), which led

to a higher CO₂ selectivity compared to that obtained for the 1.5Ru10Al catalyst (Fig. 2.d). It is important to point out that the Ru-based catalyst produced a syngas richer in H₂ and selective to CO compared to the Rh-based catalyst one. For this reason, Ru was selected as the active metal phase for further investigations.

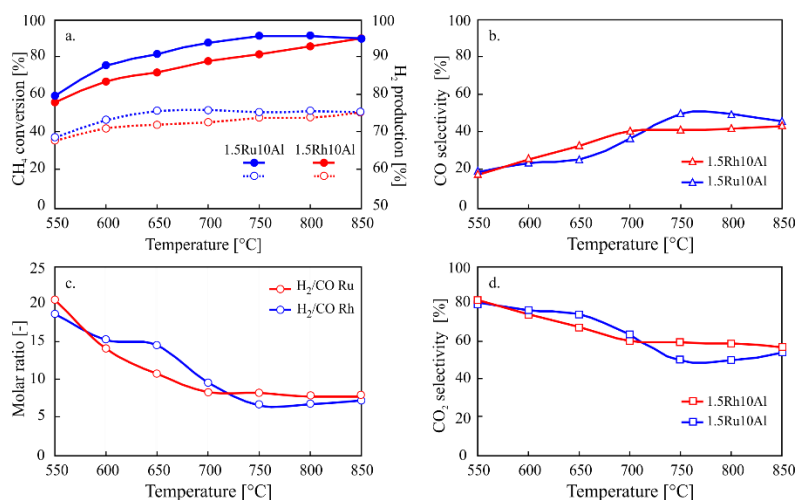


Fig. 2. MSR tests, performance comparison of monoliths 1.5% Ru and 1.5% Rh on 10% γ -Al₂O₃ at WHSV = 750 and S/C = 3. a) CH₄ conversion and H₂ production; b) CO selectivity; c) H₂/CO molar ratio, and d) CO₂ selectivity.

3.2. Ru/ γ -Al₂O₃ catalyst: loading comparison

The effect of catalyst loading on catalytic performance of Ru/ γ -Al₂O₃ for MSR was studied by varying the amount of both the carrier and the active metal phase. Three different loads of γ -Al₂O₃ (5, 10, and 20 wt.%), corresponding to 3.20, 6.45, and 12.89 mg cm⁻², respectively, were studied. Ru, as the noble metal phase, was loaded on γ -Al₂O₃ with two different percentages of active phase (1.5 and 3.0 wt.%, respectively) corresponding to a catalyst mass loading of 3.20 mg cm⁻². All experiments were carried out in the temperature range of 550 to 850 °C, with fixed S/C molar ratio of 3.0 and volumetric flow equal to 32.65 NL h⁻¹.

Fig. 3 (a-d) shows the effect of the carrier and active phase loading on the catalytic performance of the various catalytic monoliths. The results pointed out that the best catalytic performance was obtained with a load of 6.45 mg cm⁻² (corresponding to 10 wt.% of γ -Al₂O₃ and 1.5 wt.% of Ru, sample 1.5Ru10Al), where the maximum CH₄ conversion achieved was 91 % at 800 °C (Fig. 3.a). On the other hand, H₂ concentration was quite stable for all catalyst at temperatures from 650 to 850 °C, with a H₂ production higher than 60 %, except for 1.5Ru5Al catalyst (Fig. 3.b), where the highest concentration of H₂ reached was 43.22 %. Analyzing the selectivity of CO and the H₂/CO molar ratio (Fig. 3.c and 3.d), the highest concentration in dry reformat of CO was obtained for 1.5Ru10Al catalyst over the

entire temperature range studied. Interestingly, for the catalysts with mass loading of 3.2 mg cm^{-2} (corresponding to 5 wt. % of Al_2O_3 on the bare monolith), the catalytic performance was significantly improved with increasing metal loading (from 1.5 to 3 wt.%). In fact, the maximum CH_4 conversions reached at 800°C for 1.5Ru5Al and 3Ru5Al catalysts were 48.19 % and 69.24 %, respectively. Thus, the 3Ru5Al catalyst showed the second highest production of H_2 and CO selectivity after the 1.5Ru10Al one. It is also important to note that all catalysts studied showed similar CO selectivity (23.37–27.08 %) at 650°C . Comparing with the results obtained by Amjad et al. [21] for Ru/ Al_2O_3 catalyst powder, similar results were reached in terms of CH_4 conversion, H_2 production, and CO selectivity in the temperature range of 550 to 650°C . Thus, according to our previous work [39], it is possible to conclude that by increasing catalyst loading by more than 10 mg cm^{-2} , the catalytic performance towards the MSR reaction decreases. This result can be explained considering that an excess of Al_2O_3 carrier, which leads to a thicker layer covering the monolith walls, could not participate in the catalytic reaction and may even decrease both the dispersion of the noble metal and the number of active sites. Besides, it is well known that higher catalyst loadings lead to higher coating thickness and, therefore, a higher intraparticle mass transfer resistance, worsening the overall catalyst performance [40–42]. In the following section, we highlight in depth the mass transfer effects on structured monolith catalyst.

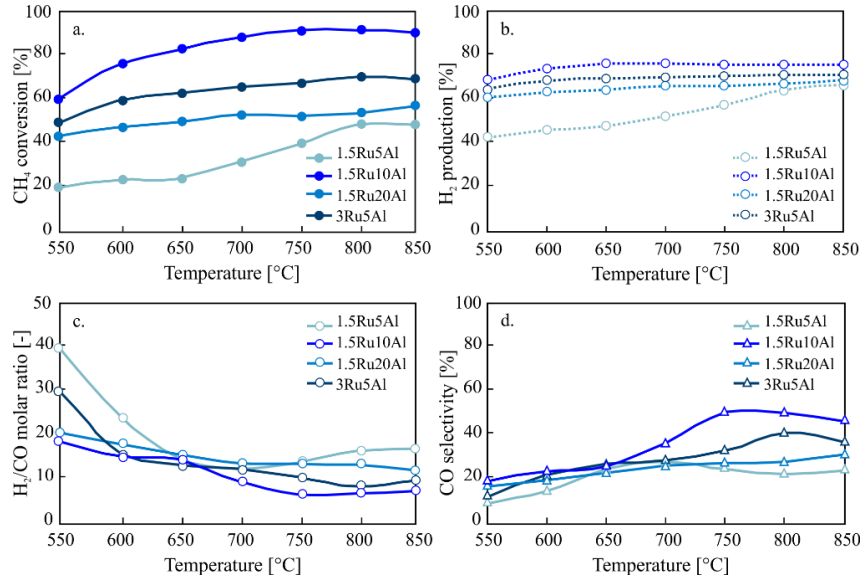


Fig. 3. MSR tests, performance comparison at WHSV = 750 and 3 S/C = 3 of Ru/ γ - Al_2O_3 monoliths with different catalyst loadings: a) CH_4 conversion; b) H_2 production; c) H_2/CO molar ratio; d) CO selectivity.

3.4. Mass transfer effects on Ru/γ-Al₂O₃ structured monolith catalyst

It is well known that the performance of a catalytic monolith involves a combination of reaction and transport processes, where the reactants and products undergo a series of steps over the catalyst, including: 1. diffusion of the reactants from the bulk gas phase to the external surface of the structured catalyst (external or inter-phase diffusion); 2. diffusion of the reactants into the catalyst pores to the active sites (internal or intra-phase diffusion); 3. adsorption of the reactants onto active sites; 4. reaction at specific active sites on the catalyst surface; 5. desorption of products from catalyst sites; 6. diffusion of the products through the catalyst pores (internal or intra-phase diffusion) and 7. diffusion of the products across the boundary layer surrounding the structured catalyst (external or inter-phase diffusion) [43–45].

According to the literature, three main regimes of catalytic rate control can exist in a coated monolith: (i) external/inter-phase diffusion regime (steps 1 and 7); (ii) internal/intra-phase diffusion regime (steps 2 and 6); and kinetic regime (steps 2 and 6) of the catalyst performance. Joshi et al. [46] developed a low-dimensional (LD) model to analyze catalytic reactions in washcoated monolith with channels of arbitrary shape. The LD model was derived directly by averaging the governing equations and using the concept of internal and external mass transfer coefficients, which were expressed in terms of three concentrations and two temperature modes and include washcoat diffusional effects without using the concept of effectiveness factor. Moreover, a practical criterion was developed to determine the transition between various controlling regimes in terms of resistances or concentration ratios [47]. We used this criterion to quantify the relative importance of reaction, pore diffusion, and external mass transfer processes in a coated monolith by SCS. Firstly, we defined the characteristic length scales for transverse diffusion associated within gas phase ($R_{\Omega,e}$) and catalytic layer ($R_{\Omega,i}$) in a monolith of square channel and circular diameter with a coated layer for the case of first order reaction. Then, we determined the external mass transfer coefficient ($k_{m,e}$) between the bulk of gas phase and the fluid-catalytic layer interface as [48]:

$$k_{m,e} = \frac{Sh_e \cdot D_{CH_4-mix}}{4 \cdot R_{\Omega,e}} \quad (12)$$

and the internal mass transfer coefficient ($k_{m,i}$) between the gas-catalytic layer interface and bulk of catalytic layer as:

$$k_{m,i} = \frac{Sh_i \cdot D_e}{R_{\Omega,i}} \quad (13)$$

where D_f is the molecular diffusivity of the reactant in gas phase ($m^2 s^{-1}$), D_e is the effective diffusivity of CH₄ within coated layer ($m^2 s^{-1}$), Sh_e and Sh_i are the external and internal Sherwood numbers, respectively. To determine Sh_e we considered the approximation proposed by Balakotaiah and West [49] used for any arbitrary geometry:

$$Sh_e = Sh_{e,\infty} + \frac{2.8}{Sc^{\frac{1}{6}}} \sqrt{P} \quad (14)$$

where $Sh_{e,\infty}$ is the asymptotic external Sherwood number ($Sh_{e,\infty} = 2.98$ for square channel), Sc is the Schmidt number, and P is the transverse Peclet number calculated as [50, 51]:

$$P = \frac{R_{\Omega,e}^2 \cdot u}{L \cdot D_{CH_4-mix}} \quad (15)$$

To estimate Sh_i we used the correlation proposed by Balakotaiah et al. [52]:

$$Sh_i = Sh_{i,\infty} + \frac{\Lambda \phi^2}{1 + \Lambda \phi} \quad (16)$$

where $Sh_{i,\infty}$ is the asymptotic internal Sherwood number, ϕ is the Thiele modulus and Λ is a constant that depends on the coated layer geometric and kinetic parameter [48]. Table 2 shows the effective diffusion lengths, asymptotic external and internal Sherwood numbers and Λ for the channel shape and flow area under consideration. Thus, considering the following assumptions: 1. laminar and fully developed flow, 2. the hydraulic diameter of the channel much smaller than the length of cordierite monolith 3. isothermal conditions, and 4. first order kinetic; we expressed the overall resistance for mass transfer in a coated monolith by SCS according to Balakotaiah et al. [47] as:

$$R_t = R_e + R_i + R_r \quad (17)$$

$$\text{a. } R_e = \frac{4 \cdot R_{\Omega,e}}{Sh_e \cdot D_{CH_4-mix}} \quad \text{b. } R_i = \frac{R_{\Omega,i}}{Sh_i \cdot D_e} \quad \text{c. } R_r = \frac{1}{k_r \cdot R_{\Omega,i}} \quad (18)$$

with R_e resistance for external mass transfer ($s \cdot m^{-1}$), R_i resistance for internal mass transfer ($s \cdot m^{-1}$), R_r resistance for MSR reaction ($s \cdot m^{-1}$), and R_t overall resistance for MSR process ($s \cdot m^{-1}$).

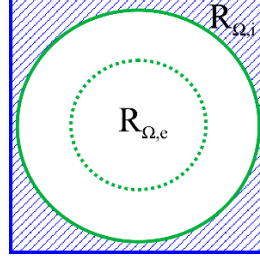


Fig. 4. Definition of the characteristic length scales for transverse diffusion associated within gas phase ($R_{\Omega,e}$) and catalytic layer ($R_{\Omega,i}$) in a monolith of square channel and circular diameter with a coated layer.

To characterize the flow and the reactions the following five characteristic times are used [49, 53, 54]:

$$t_c = \frac{L}{u} \quad t_z = \frac{L_m^2}{D_{CH_4-mix}} \quad t_d^e = \frac{R_{\Omega,e}^2}{D_{CH_4-mix}} \quad t_d^i = \frac{\delta_c^2}{D_e} \quad t_r = \frac{C_{CH_4,in}}{r_{CH_4} \cdot \rho_c} \quad (19)$$

where t_c is the convection (or residence) time, t_z is the longitudinal diffusion time for the flow area, t_d^e is the transverse diffusion time for the flow area, t_d^i is the transverse diffusion time for the coated area, and t_r is the reaction time.

Catalyst	$R_{\Omega,e}$ [mm]	$R_{\Omega,i}$ [mm]	$Sh_{e,\infty}$	$Sh_{i,\infty}$	Λ
1.5Ru5Al	0.45	0.188	2.98	1.836	1.2
3Ru5Al	0.4508	0.1865	2.98	1.836	1.2
1.5Ru10Al	0.435	0.225	2.98	1.836	1.2
1.5Ru20Al	0.4	0.3182	2.98	2.533	0.73

Table 2. Effective diffusion lengths, asymptotic external and internal Sherwood numbers and Λ for square channel shape and circular flow area for the different catalyst studied.

In fig. 5 (a-d) we show the effect of $\gamma\text{-Al}_2\text{O}_3$ amount on the controlling regimes towards MSR reaction on the prepared coated monolith catalysts. For all the catalysts studied, the resistances to mass transfer (inter/intra-phase diffusion) are much less temperature sensitive, since the diffusivities of reacting species in the gas phase (D_{CH_4-mix}) and in the coated layer (D_e) are much weaker functions of temperature in comparison to the reaction resistance, which is strongly dependent on Arrhenius equation. Thus, the interphase and intraparticle mass transfer rates increase only slightly with temperature. Therefore, as the catalyst temperature is

increased, the reaction rate increases exponentially, the reaction resistance becomes less dominant and the mass transfer resistances become important.

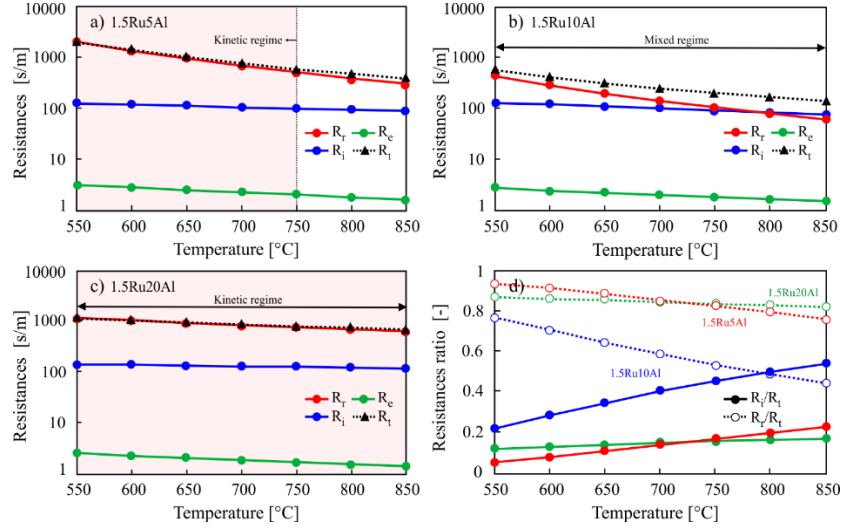


Fig. 5. Definition of the characteristic length scales for transverse diffusion associated within gas phase ($R_{Q,e}$) and catalytic layer ($R_{Q,i}$) in a monolith of square channel and circular diameter with different coating: a) 1.5Ru5Al; b) 1.5Ru10Al; c) 1.5Ru20Al; d) resistance ratios for all catalysts loading.

When comparing the effect of $\gamma\text{-Al}_2\text{O}_3$ amount on the controlling regimes in catalytic monoliths, the 1.5Ru5Al monolith operates in a kinetic regime at temperatures lower than 750 °C (Fig.5.a). By increasing the $\gamma\text{-Al}_2\text{O}_3$ loading to 20 wt.% (1.5Ru20Al catalyst), the process is completely controlled by the reaction for the entire temperature range studied (Fig.5.c). As a result, a nearly uniform concentration profile prevails in the transverse direction of the structure (fig 6). Thus, when the catalytic performance of MSR reaction is solely governed by the reaction kinetics, the total resistance (R_t) is practically equal to the reaction resistance and the R_r/R_t ratio is greater than 0.8 (Fig 5.d). Besides, as expected, when the monolith operates in a kinetic regime, the characteristic times for the MSR reaction are much larger than that for the external and internal mass transfer diffusion (see Table S.I X). On the other hand, for the 1.5Ru10Al catalyst (10 wt.% of alumina, 6.45 mg cm^{-2}), the monolith operates in a mixed regime for all temperature range studied, in which both the kinetic and the intraparticle diffusion co-exist (fig.5.a), with both R_r/R_t and R_i/R_t lower than 0.8. By observing the catalytic performance for the different loading of $\gamma\text{-Al}_2\text{O}_3$ (Fig. 3), it is worth noting that for the 1.5Ru20Al catalyst, the conversion of CH_4 increases slightly with temperature, being practically steady for the temperature range under consideration. This effect explains why the reaction resistance is practically independent with temperature.

On the contrary, for the 1.5Ru10Al catalyst, CH₄ conversion increases more rapidly with temperature up to 750 °C, and then remains slightly stable.

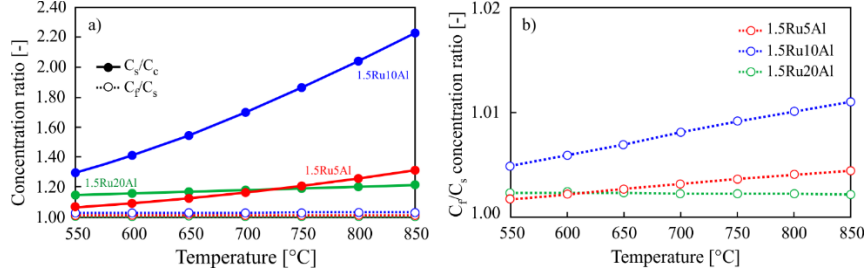


Fig. 6. Concentration ratios for the various catalysts tested.

To gain insight into the catalyst activity by varying the γ -Al₂O₃ content, we evaluated the Thiele modulus (ϕ) and the effectiveness factor (η) for a first-order kinetics reaction, according to the following equations [47, 48]:

$$\phi = \sqrt{\frac{k_r \cdot R_{\Omega,i}^2}{D_e}} \quad \eta = \frac{1}{1 + \frac{\phi^2}{Sh_i}} \quad (20)$$

where k_r is the observed first-order reaction rate constant (s⁻¹), $R_{\Omega,i}$ the effective transverse diffusion length in the coated catalyst layer for the internal resistance (m), D_e is the effective diffusivity of CH₄ (m² s⁻¹), and Sh_i is the internal Sherwood number. All the correlations and physical parameters used for the calculations of ϕ and η are available in the Appendix. Fig.7 shows the effectiveness factor as a function of Thiele modulus for the different catalyst loadings. As expected, the effectiveness factor for the case of slow reaction $\phi \ll 1$ tends to unit. In particular, the 1.5Ru20Al catalyst showed a variation of ϕ much less sensitive to temperature ($0.82 < \phi < 0.87$) than the other catalyst loadings, indicating that the process is rate-limited and the reaction rate is controlled by the intrinsic kinetics.

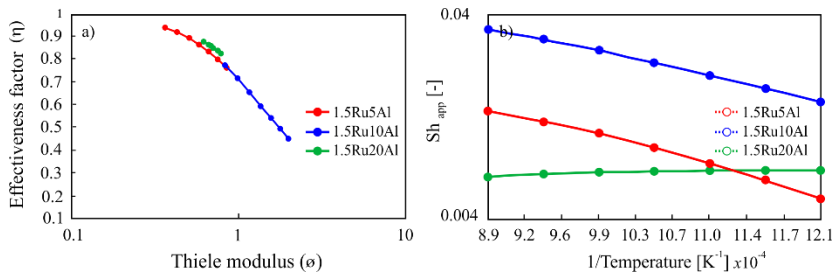


Fig. 7. Effectiveness factor (a) and apparent Sherwood number (b) for the various coated monoliths.

Additionally, we plot the experimentally observable overall Sherwood number (Sh_{app}) calculated using Eqn. 21 as a function of reciprocal of temperature on a logarithmic scale (Fig. 7b). The theoretical upper limit for Sh_{app} ($Sh_{e,\infty}$) is 2.98 for the channel shape under consideration (square channel with circular flow area) [50, 51].

$$\frac{1}{Sh_{app}} = \frac{1}{Sh_e} + \frac{\mu\lambda}{4} \cdot \frac{1}{Sh_i} + \frac{\mu\lambda}{4\phi^2} \quad (21)$$

$$\mu = \frac{R_{\Omega,i}}{R_{\Omega,e}} \quad \lambda = \frac{D_f}{D_e} \quad (22)$$

It is evident from the results that the experimental conditions used lead to rather low values of Sh . Bennett et al. [55] reported a value of Sh_{app} as small as 0.05, which was attributed to the low activation energies and pre-exponential factors obtained for the catalytic oxidation of propane. Similar results were obtained by Joshi et al. [56] for the case of hydrogen oxidation on Pt, which presents a very low intrinsic activation energy ($\sim 9 \text{ kJ mol}^{-1}$), obtaining experimental Sherwood numbers (Sh_{app}) less than 0.55. In our study, the apparent activation energies obtained for the MSR reaction were determined from the conversion data ($X_{CH_4} < 5 \%$) for the different catalyst loads ($Ea_{app} \approx 50 \text{ kJ mol}^{-1}$). These values are low compared to other activation energies on supported Ru catalyst for MSR reaction [57, 58]. As shown in Fig. 7b, low Sh_{app} values (below 0.035) are obtained for the three catalysts studied, especially for 1.5Ru20Al catalyst.

On the other hand, it is interesting to note that the ratios of reactant diffusivities in the gas phase and the coated layer (μ) obtained in our study are greater than 225. Joshi et al. [48] studied the variation of Sh_{app} for the different controlling regimes by varying the values of μ for circular channel with circular flow area. They obtained that for values of diffusivity ratios higher than 200, the Sh_{app} for $\phi \ll 1$ (slow reaction) are much lower than 0.1 ($\sim 10^{-2}$ - 10^{-3}), as obtained in this study.

To study the effect of WHSV and S/C molar ratio on the controlling regimes in a coated monolith by SCS, we selected the 1.5Ru10Al catalyst according to the best results obtained in terms of CH_4 conversion, H_2 production, and CO selectivity. The 1.5Ru10Al catalyst was studied at space velocities of 750, 1,500, and 3,000 $NL \text{ h}^{-1} \text{ g}_{cat}^{-1}$, calculated on metal basis, and S/C molar ratio of 3 and 3.2 respectively. As visible in Fig. 8, as the S/C molar ratio increases, both the mass transfer resistances and the reaction resistance increase. In particular, R_r for the S/C molar ratio of 3.2 is about 1.5 times higher than that obtained at S/C 3 for the entire temperature range studied. Since the catalytic performance decreased as the S/C molar ratio increased (Fig. A1), lower rate constants (k_r^{obs}) were obtained for S/C equal to 3.2, thus increasing the reaction resistance. Since a higher bulk reaction controlling is obtained either by increasing the S/C molar ratio as the WHSV, a concentration profile closer to the unit exists in the transverse direction of the monolith (Fig. 8b).

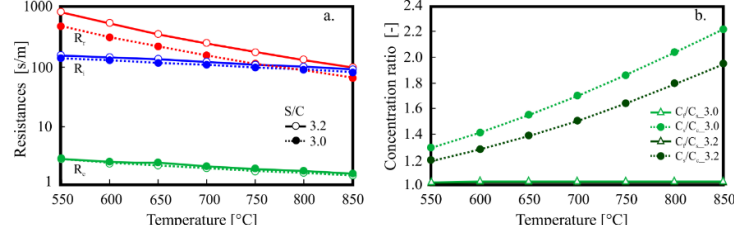


Fig. 8. Resistances (a) and concentration ratios for different S/C values for the 1.5Ru10Al coated monolith.

3.5. Heat transfer effects on Ru/ γ -Al₂O₃ structured monolith catalyst

For heterogeneous catalytic processes, heat management in chemical reactions is a very important aspect for both reactor design and overall performance of the process. In addition to mass transfer effects, heat transfer effects can also occur in heterogeneous catalysis for reactions with a significant heat of reaction, either exothermal or endothermal such as combustion or steam reforming [45, 59, 60]. External temperature gradients between the bulk of the fluid phase and the surface of the catalytic layer are originated from the reaction enthalpy associated with surface reaction. The external temperature difference can be large even when mass transfer limitations are negligible, which disguises the actual reaction kinetics occurring at surface temperature (T_s) and not at the bulk of the fluid phase temperature (T_b). The surface temperature can be determined by the heat balance at steady state conditions, assuming that the outer surface of the catalyst layer is uniformly available for the reactants. In this way, each section of the outer surface behaves kinetically in the same way as all other parts, thus the steady-state analysis of that system is essentially one-dimensional [45, 59]. For more details of the heat balance go to the supplementary information section. We report the final expression of the heat balance using the Chilton-Colburn analogies between mass and heat transfer:

$$(T_b - T_s) = \left(\frac{\Delta H_r \cdot C_b}{\rho_f \cdot c_{p,f}} \right) \cdot Le^{-2/3} \cdot Ca \quad (23)$$

$$Le = \frac{Sc}{Pr} ; \quad Ca = \frac{c_b - c_s}{c_b} \quad (24)$$

where T_b, T_s is the temperature in the bulk of the gas phase and surface of the catalyst layer (K) respectively, ΔH_r is the heat of MSR reaction (J mol⁻¹), C_b is the concentration in the bulk of the gas phase (mol m⁻³), ρ_f is the density of the gas phase (Kg m⁻³), $c_{p,f}$ is the heat capacity of the gas phase (J Kg⁻¹ K⁻¹), Le is the fluid Lewis number, Pr is the Prandtl number and Ca is the Carberry number. Thus, by dividing Equation 23 by T_b , it is possible to obtain the dimensionless external Prater

number which represents the ratio of the maximum heat consumption and heat transfer rates:

$$\beta_{ext} = \frac{\Delta T_{ad}}{T_b} \cdot Le^{-2/3} = \left(\frac{\Delta H_r \cdot C_b}{\rho_f \cdot c_{p,f}} \right) \cdot \frac{1}{T_b} \cdot Le^{-2/3} \quad (25)$$

The interphase heat transfer limitations can be evaluated using the criterion derived by Mears [61] (Eq. 26) with the perturbation approach, in which the heat transfer resistance of the fluid phase is assumed to be lumped at the surface. We use this criterion to estimate the external heat transfer effects by varying the alumina content in the monolithic catalyst:

$$\chi = \frac{(\Delta H \cdot R^{obs, R\Omega e})}{h_e \cdot T_b} < \frac{0.15}{\gamma_b}; \quad \gamma_b = \frac{E_{act}}{R_g \cdot T_b} \quad (26)$$

where R^{obs} is the observed reaction rate ($\text{mol m}^3 \text{s}^{-1}$), h_e is the heat transfer coefficient associated for the gas phase ($\text{W m}^{-2} \text{K}^{-1}$), R_g is the gas constant ($\text{J mol}^{-1} \text{K}^{-1}$), E_{act} is the apparent activation energy of the reaction (J mol^{-1}), χ is the Damkholder for interphase heat transport and γ_b is the Arrhenius number evaluated at the bulk of the gas phase.

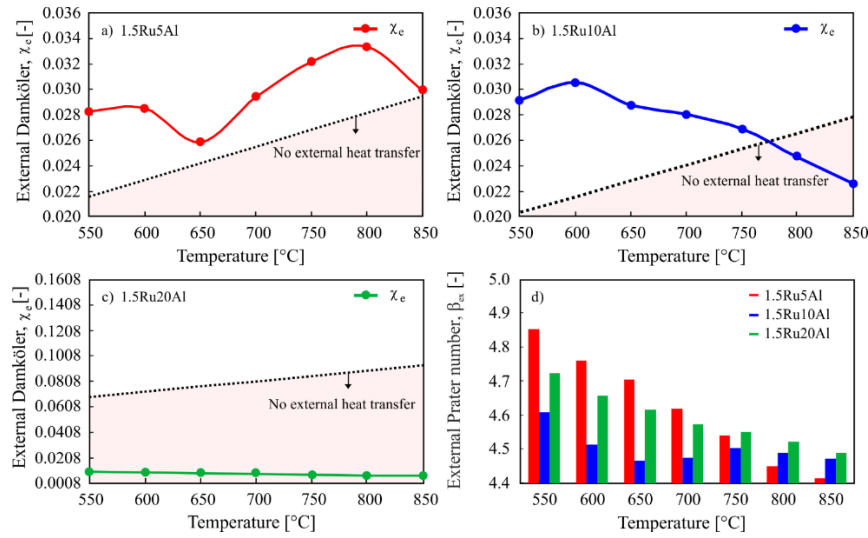


Fig. 9. External Damköhler numbers in a monolith of square channel and circular diameter with different coating: a) 1.5Ru5Al; b) 1.5Ru10Al; c) 1.5Ru20Al. External Prater number for the various catalysts loading (d).

As observed in Fig. 9, for the 1.5Ru5Al2O3 catalyst, external heat transfer limitations are presented for the complete temperature range studied, while for the 1.5Ru10Al catalyst the thermal effects are important a temperature below 725°C. On the other hand, not interphase heat transfer limitations are observed for the higher catalyst loading. It is important to note that for the lower alumina content the temperature difference between the bulk of the gas phase and the surface of the catalytic layer increases considerably as the inlet gas temperature increases from 650-800 °C, and then start to decrease probably as mentioned above, in this temperature range initiates the WGS reaction which is exothermic and leads to an increase in the T_s . For catalysts with 10 and 20 wt.% of alumina, the ΔT is practically constant as the temperature of the reactant gas increases, approximately 70 and 25 K respectively. It is also important to point out that the temperature difference between bulk and outer catalytic layer surface is directly proportional to the heat of MSR reaction per mol of diffusing reactant and the fractional drop in concentration between the bulk of the gas phase and the surface of the catalyst layer (see eq. 23). Thus, the quotient of the heat consumed by complete reaction of unit volume of reacting gas mixture ($\Delta H_r \cdot C_b$) and the volumetric heat capacity of the reacting mixture ($\rho_f \cdot c_{p,f}$) gives the temperature rise equivalent to complete adiabatic conversion of the reacting mixture when C_s is zero. The eq. 23 also shows that heat transfer limitation and ΔT may be significant if ΔH_r values are large, even when concentration gradients are small as those obtained in section 3.4 for all the alumina loading studied. Since the MSR reaction is highly endothermic, the temperature of the catalyst surface will be less than in the bulk fluid phase, and the observed rate will be less than that corresponding to the bulk-fluid temperature. In addition to the interphase heat transfer limitations, a large number of highly exothermic and endothermic catalytic reactions are accompanied by internal thermal effects, particularly for relatively fast intrinsic kinetics. Anderson in 1963 [62] applied the perturbation approach to derive a criterion for the lack of importance of temperature gradients in catalyst particles. The reaction is assumed to follow Arrhenius temperature dependence and this criterion is valid regardless of whether there are diffusion limitations in the particle or not. Thus, we use this criterion to evaluate the intraparticle heat transfer effects by varying the alumina content in the structured catalyst:

$$\frac{(\Delta H \cdot R^{obs} \cdot R_{\theta l}^2)}{\lambda_{cat} \cdot T_s} < \frac{0.75}{\gamma_s} \quad (27)$$

$$\psi = \frac{(\Delta H \cdot R^{obs} \cdot R_{\theta l}^2)}{\lambda_{cat} \cdot T_s}; \quad \gamma_s = \frac{E_{act}}{R_g \cdot T_s} \quad (28)$$

where λ_{cat} is the thermal conductivity of the Ru/Al₂O₃ catalyst (W m⁻¹ K⁻¹), ψ is the Damkohler for intraparticle heat transport and γ_s is the Arrhenius number evaluated at the surface of the gas phase. As observed from the Fig. 10 (a-c), for all the catalyst loading studied $\psi \ll \frac{0.75}{\gamma_s}$ indicating that the absence of intraparticle

heat transfer. This can also be observed by studying the temperature gradients within the catalytic layer using the relationship originally derived by Damköhler in 1943 [63], which is valid for all the kinetics and applies to all the particle geometries assuming that T_s and C_s are uniform over the entire boundary surface [45]:

$$(T_s - T_{b,c}) = (\Delta H_r) \cdot \frac{D_e}{\lambda_e} \cdot (C_s - C_{b,c}) \quad (29)$$

where $T_{b,c}$ is the temperature in the bulk of the catalyst layer (K), $C_{b,c}$ is the concentration within the catalyst layer and λ_e is the effective thermal conductivity. It is worth noting the largest possible temperature difference into the catalyst layer is attained when the concentrations within the bulk of the catalyst layer becomes zero, hence we can refer the maximum temperature difference (ΔT_{max}) to the surface temperature using the dimensionless internal Prater number (β_{in}) by [45, 59]:

$$\beta_{in} = \frac{\Delta T_{max}}{T_s} = \frac{(\Delta H_r) \cdot C_s}{T_s} \cdot \frac{D_e}{\lambda_e} \quad (30)$$

As shown in Fig. 10 d, all β_{in} values are much smaller than one, indicating the absence of temperature gradients within the catalytic layer, confirming in this way the results obtained by using the Anderson criterion.

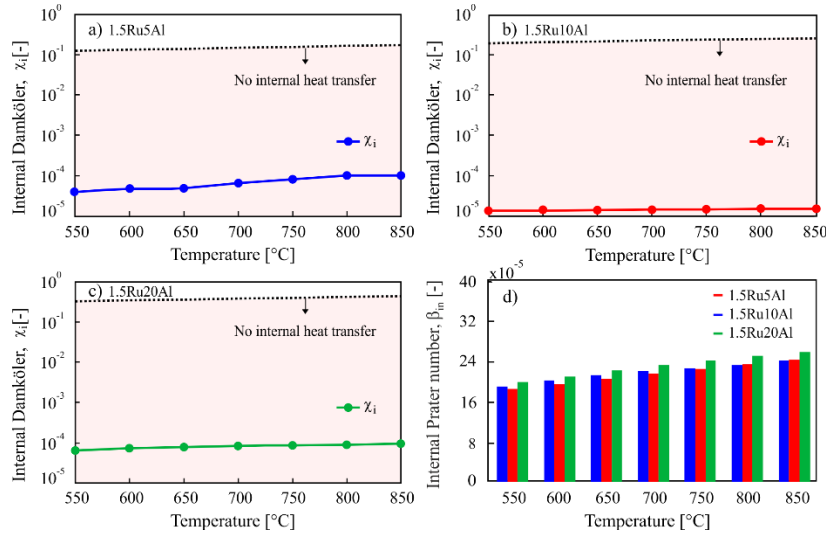


Fig. 10. Internal Damköhler numbers in a monolith of square channel and circular diameter with different coating: a) 1.5Ru5Al; b) 1.5Ru10Al; c) 1.5Ru20Al. Internal Prater number for the various catalysts loading (d).

In the following section, we will discuss the results obtained of the physico-chemical characterization on the best catalyst-selected.

3.6 Characterization of powdered catalyst and coated structured supports.

Table 3 shows the specific surface area (S_{BET}) of powder samples, bare and coated monoliths. Comparing with the pure powder of γ - Al_2O_3 , the S_{BET} of 1.5 wt.% Ru/ γ - Al_2O_3 powder catalyst was decreased by 82.6%, to $191.5 \text{ m}^2 \text{ g}^{-1}$. Instead, considering the practically zero S_{BET} of the bare monolith, As expected, the deposition of γ - Al_2O_3 on the monolith, as carrier of Ru (the active metal) notably increased the S_{BET} of the bare monolith.

Catalyst	$S_{BET} [\text{m}^2 \text{ g}^{-1}]$
γ - Al_2O_3 powder	231.7 [39]
Ru/ γ - Al_2O_3 powder	191.5 [21]
1.5 wt. % Ru/ γ - Al_2O_3 on cordierite monolith	23.8
Bare cordierite monolith	0.009

Table 3. Specific surface area values of different types of catalysts.

Ru metal dispersion and crystallite size obtained from H_2 chemisorption were 5.3% and 25 nm, respectively. Similar results were obtained in our previous work in terms of crystal size [33], while a greater dispersion of Ru is obtained when the catalyst is prepared in a single step by SCS.

Fig. 11 shows the XRD diffraction patterns of the 1.5 wt.% Ru/ γ - Al_2O_3 catalyst, compared with the reference patterns of γ - Al_2O_3 and RuO_2 . The diffractogram shows the peaks related to the Ru in its oxidized form (RuO_2 JCPDS database, ref. 00-002-1365) and the γ - Al_2O_3 in its amorphous structure (JCPDS database, ref. 00-001-1243).

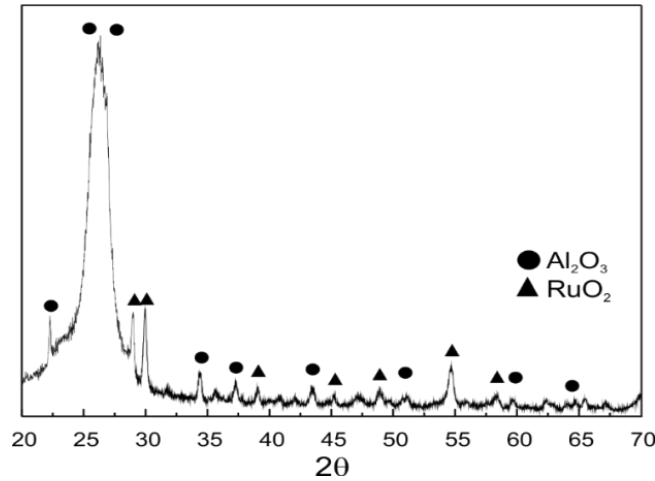


Fig. 11. XRD patterns of 1.5 wt.% Ru/ γ -Al₂O catalyst, with the reference peaks of RuO₂ (JCPDS database, ref. 00-002-1365) and γ -Al₂O₃ (JCPDS database, ref. 00-001-1243).

Figure 12 shows FESEM images of the coated monolith. There is a good dispersion of the catalytic particles on the surface of the monolith. In particular, alumina particles on the surface of the monolith are well dispersed by providing sufficient specific surface area to host Ru. Furthermore, Ru particle size distribution on Al₂O₃ particles seems to be wider. Table 4 shows the EDX analysis coupled with FESEM, giving evidence of the presence of Ru particles and alumina.

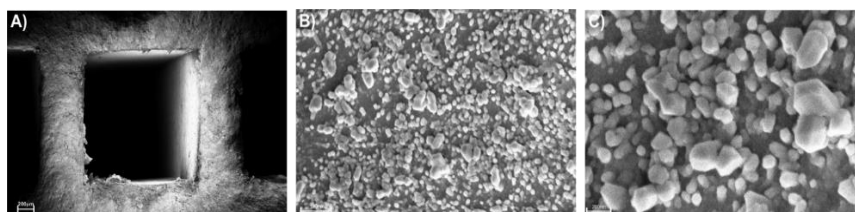


Fig. 12. FESEM images of 1.5% Ru on 10% alumina on 100 cpsi monolith at different magnifications. **A)** 100X, **B)** 50000 kX, **C)** 150000 kX.

Element	Weight %	Atomic %
O	53.45	68.56
Mg	1.09	0.92
Al	34.88	26.50
Si	5.54	2.58
Ru	7.04	1.44
Tot	100.00	100.00

Table 4. EDX analysis of the 100 cpsi monolith coated with 1.5% Ru on 10% alumina.

3.7 Ageing test on the best performing coated monolith.

After performing various experiments, the catalyst 1.5Ru10Al performed best in all types of test. The conversion remained higher than the others and it showed high productivity and higher CO selectivity at low WHSV for temperatures between 600-750°C and S/C 3. The most competitive catalyst with the same experimental conditions was Rh, but it was clearly seen that the difference in performance was almost more than 8%.

Furthermore, a new cordierite monolith was coated with the best catalyst, 1.5%Ru/10%Al₂O₃, and its catalytic performance was evaluated with respect to

time. Figure 13 shows methane conversion versus the time on stream (TOS), at two different WHSV. In the first 30 hrs, reaction conditions were fixed at 800 °C, WHSV = 750 and S/C = 3. Then, for the next 20 hrs, WHSV was increased to 1500, and finally reduced again to 750 (being T and S/C always constant at 800 °C and 3, respectively). Clearly, the coated monolith kept methane conversion almost constant at its starting value, independent of the variation of WHSV.

Thus, this test confirms that overall at the temperature of 800 °C, even when varying the WHSV, no significant difference is recorded in methane conversion, which remained stable throughout the time period.

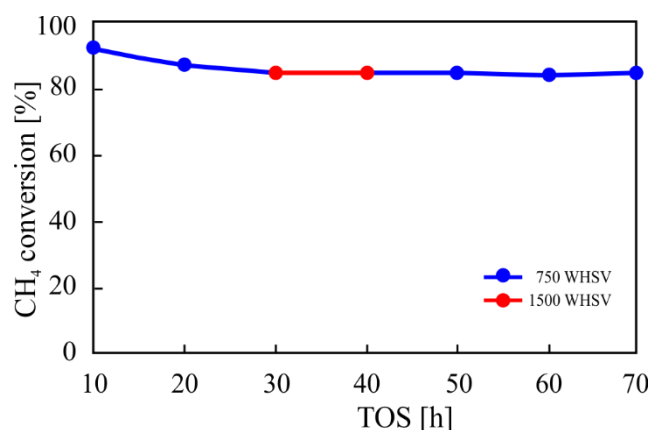


Fig. 13. Stability test of the cordierite monolith coated with 1.5%Ru/10%Al₂O₃ catalyst at 800 °C and S/C = 3. WHSV variable between 750 and 1500 $\text{Nl h}^{-1} \text{g}_{\text{cat}}^{-1}$.

4. CONCLUSION

In this study, the catalytic performance and mass/heat transfer effects were evaluated for Ru/ γ -Al₂O₃ catalyst supported on ceramic cordierite monolith towards MSR reaction. All the catalysts were prepared in a single step by solution combustion synthesis coated on over monolith of square channel with 100 cpsi. By comparing the catalytic performance of Ru and Rh as active metal phase, the Ru-based catalyst was found to be more active towards MSR reaction, showing a syngas richer in H₂ for the entire temperature range studied. The best catalyst loading of Ru/ γ -Al₂O₃ catalyst was 6.45 mg cm^{-2} , where the excess of Al₂O₃ carrier could only lead to a thicker layer and not participate in the catalytic reaction, leading to the catalyst working in an entirely kinetic regime. The temperature dependence on the external and internal diffusion regimes is much weaker compared to the reaction resistance, which is strongly dependent of the Arrhenius equation. External heat transfer limitations were presented at lower carrier content, while that low values of internal Prater numbers confirmed the absence of internal heat limitation. An

excellent stability of the 1.5% Ru on 10% Al₂O₃ catalyst (1.5Ru10Al sample) was observed over 70 h of TOS for MSR process.

5. APPENDIX

In the following, a detailed explanation of fluid and catalyst layer properties determination, characteristic time analysis, external and internal mass transfer calculations and heat transfer investigation is reported.

A.1 Estimation of fluid properties

Molecular weight (M_{mix}), density (ρ_f) and viscosity (μ_f) of gas mixture were calculated as:

$$M_{mix} = \sum_{i=1}^n y_i M_i \quad (S1)$$

$$\rho_f = \frac{P M_{mix}}{R_g T} \quad (S2)$$

$$\mu_f = \frac{\sum_{i=1}^n \mu_i y_i M_i^{1/2}}{\sum_{i=1}^n y_i M_i^{1/2}} \quad (S3)$$

where y_i is the mole fraction of the compound, M_i is the molecular weight of the compound (kg kmol⁻¹), P is the pressure (kPa), T is the absolute temperature (K), R is the universal gas constant (J mol⁻¹ K⁻¹) and μ_i is the viscosity of a single component (kg m⁻¹ s⁻¹).

Gas viscosity (μ_i , μP) of a single component was calculated as:

$$\mu_i = A + BT + CT^2 \quad (S4)$$

using the tabulated values of A, B, and C [64].

	CH ₄	H ₂ O	H ₂	CO	CO ₂
A	3.844	-36.826	27.758	23.811	11.811
B	0.40112	0.429	0.212	0.53944	0.49838
C	-0.00014303	-0.0000162	-0.0000328	-0.00015411	-0.0001085

Table A1. Values of A, B, and C used in eq. S.4.

The diffusivity of CH₄ in gas mixture (D_{CH_4-mix} , cm² s⁻¹) was calculated from the binary diffusion of CH₄ and i gas species (D_{CH_4-i}) by:

$$D_{CH_4-mix} = \frac{1 - y_{CH_4}}{\sum_{i=1, i \neq CH_4}^n \frac{y_i}{D_{CH_4-i}}} \quad (S5)$$

where D_{CH_4-i} was determined by Fuller equation (eq. S.6) [65], using tabulated values of v_i [66].

$$D_{CH_4-i} = \frac{10^{-3} T^{1.75} \left(\frac{1}{M_{CH_4}} + \frac{1}{M_i} \right)}{P \left(v_{CH_4}^{1/2} + v_i^{1/3} \right)^2} \quad (S6)$$

where v_i are tabulate in Table A2.

	CH ₄	H ₂ O	H ₂	CO	CO ₂
v_i (cm ³ ·mol ⁻¹)	24.4	12.7	7.1	18.9	26.9

Table A2. Values of v_i used in eq. S.6.

The effective diffusivity of methane ($D_{CH_4,e}$) in the catalytic layer was calculated using the following equation [67, 68]:

$$D_{CH_4,e} = \frac{\varepsilon_c}{\tau_c} \cdot \left(\frac{1}{D_{CH_4-mix}} + \frac{1}{D_k} \right)^{-1} \quad (S7)$$

where ε_c is the coated layer porosity ($\varepsilon_c = \rho_c \cdot V_{BJH}$) [69], τ is the tortuosity factor ($\tau = 2 - \varepsilon_c$) [70] and the Knudsen diffusion (D_k) was determined by eq. S.8 [71]:

$$D_k = 9700 \cdot r_p \cdot \sqrt{\frac{T}{M_{CH_4}}} \quad (S8)$$

where ρ_c (kg m⁻³) is the bulk density of the catalyst (3500 kg m⁻³), V_{BJH} is the total pore volume (cm³ g⁻¹), r_p is the pore diameter (cm) and M_{CH_4} is the molecular weight of CH₄.

The mass transfer coefficient of CH₄ (k_G , m s⁻¹) was determined from the Sherwood number (Sh) by:

$$k_G = \frac{Sh \cdot D_{CH_4-mix}}{d_h} \quad (S9)$$

where Sh is calculated from Reynold (Re) and Schmidt (Sc) numbers by Eqs. S.10, S.11 and S.12 [60, 72, 73].

$$Sh = 2.976 \cdot \left(1 + 0.095 \cdot Re \cdot Sc \cdot \frac{d_h}{L_m} \right)^{0.45} \quad (S10)$$

$$Re = \frac{d_h \cdot u_0 \cdot \rho_f}{\mu_f} \quad (S11)$$

$$Sc = \frac{\mu_f}{\rho_f \cdot D_{CH_4-mix}} \quad (S12)$$

where d_h is the hydraulic diameter of the bare monolith (m), L_m is the monolith length (m), u_0 is the inlet gas velocity at operative conditions ($m\ s^{-1}$), ρ_f is the density of gas mixture ($kg\ m^{-3}$), μ_f is the viscosity of gas mixture ($kg\ m^{-1}\ s^{-1}$) and D_{CH_4-mix} is the diffusivity of CH_4 in gas phase ($m^2\ s^{-1}$).

The inlet gas velocity at operative conditions u_0 ($m\ s^{-1}$) was calculated as:

$$u_o = \frac{F_{ch}}{A_{ch} \cdot \varepsilon} \cdot \frac{T}{T_{St}} \cdot \frac{P}{P_{St}} \quad (S13)$$

where F_{ch} is the total flow of the gas mixture for channel ($m^3\ s^{-1}$), ε is the coated monolith voidage, A_{ch} is the frontal area of the bare monolith for square channel (m^2), T_{St} (K) and P_{St} (Pa) are the standard temperature and pressure, T (K) and P (Pa) are the operative temperature and pressure.

The thermal conductivity of gas mixture (λ_{mix} , $W\ m^{-1}\ K^{-1}$) was calculated as:

$$\lambda_{mix} = \frac{\sum_{i=1}^n \lambda_i y_i M_i^{1/2}}{\sum_{i=1}^n y_i M_i^{1/2}} \quad (S14)$$

where λ_i is the thermal conductivity of a single component ($W\ m^{-1}\ K^{-1}$) calculated as:

$$\lambda_i = A + BT + CT^2 \quad (S15)$$

using the tabulated values of A, B, and C [64].

	CH ₄	H ₂ O	H ₂	CO	CO ₂
A	-0.00935	0.00053	0.03951	0.00158	-0.01200
B	1.4028E-04	4.7093E-05	4.5918E-04	8.2511E-05	1.0208E-04
C	3.3180E-08	4.9551E-08	-6.4933E-08	-1.9081E-08	-2.2403E-08

Table A3. Values of A, B, and C used in eq. S.15.

The heat capacity of the gas mixture (Cp_f , $J\ mol^{-1}\ K^{-1}$) was calculated as:

$$Cp_f = \frac{\sum_{i=1}^n Cp_i y_i M_i^{1/2}}{\sum_{i=1}^n y_i M_i^{1/2}} \quad (S16)$$

where Cp_i is the heat capacity of a single component ($J\ mol^{-1}\ K^{-1}$) calculated as [64]:

$$Cp_i = A + BT + CT^2 + DT^3 + ET^4 \quad (S17)$$

	CH ₄	H ₂ O	H ₂	CO	CO ₂
A	34.942	33.933	25.399	29.556	27.437
B	-3.9957E-02	-8.4186E-03	2.0178E-02	-6.5807E-03	4.2315E-02
C	1.9184E-04	2.9906E-08	-3.8549E-05	2.0130E-05	-1.9555E-05
D	-1.5303E-07	-1.7825E-08	3.188E-08	-1.2227E-08	3.9968E-09
E	3.9321E-11	3.6942E-12	-8.758E-12	2.2617E-12	-2.9872E-13

Table A4. Values of A, B, C, D, and E used in eq. S.17.

A.2 Estimation of coated layer properties

Specific surface area ($SA_{BET} = 23.79 \text{ m}^2 \cdot \text{g}^{-1}$) was determined from Brunauer-Emmett-Teller (BET) and Barrett-Joyner-Halenda (BJH) analytic methods for N₂ adsorption-desorption isotherms. Pore radius ($r_p = 100 \text{ \AA}$) was given by $2PV_{BJH}/SA_{BET}$ equation.

A.3 Characteristic time analysis

The characteristic contact time, or residence time (t_c , s) is determined by [73]:

$$t_c = \frac{L_m}{u_o} \quad (\text{S18})$$

where L_m is the monolith length (m) and u_o is the inlet gas velocity at operative conditions (m s^{-1}).

The transverse diffusion time for the flow area (t_d^e , s) is determined by [73]:

$$t_d^e = \frac{R_{\Omega e}^2}{D_{CH_4-mix}} \quad (\text{S19})$$

where $R_{\Omega e}$ is the characteristic length scale for the fluid phase (m) and D_{CH_4-mix} is the diffusivity of CH₄ in gas phase ($\text{m}^2 \text{ s}^{-1}$).

The transverse diffusion time for the coated area (t_d^i , s) is determined by [73]:

$$t_d^i = \frac{\delta_c^2}{D_{CH_4,e}} \quad (\text{S20})$$

where $D_{CH_4,e}$ is the effective diffusivity of CH₄ in the coated layer ($\text{m}^2 \text{ s}^{-1}$) and δ_c is the coated layer thickness (m) calculated as [47]:

$$\delta_c = \frac{l_w^2 - \frac{\pi}{4} d_f^2}{\pi \cdot d_f} \quad (\text{S21})$$

where l_w (m) is the channel width and d_f (m) is the average channel dimension estimated by SEM.

The characteristic reaction time t_r (s) is determined by [73]:

$$t_r = \frac{C_{CH_4, in}}{r_{CH_4} \cdot \rho_c} \quad (S22)$$

where $C_{CH_4, in}$ is the concentration of CH_4 in the feed mixture (kmol m^{-3}), r_{CH_4} is the observed reaction rate for CH_4 ($\text{kmol m}^{-3} \text{s}^{-1}$), and ρ_c is the density of the catalytic layer (kg m^{-3}).

The longitudinal diffusion time t_z (s) is determined by [49]:

$$t_z = \frac{L_m^2}{D_{CH_4-mix}} \quad (S23)$$

where L_m is the monolith length (m) and D_{CH_4-mix} is the diffusivity of CH_4 in gas phase ($\text{m}^2 \text{s}^{-1}$).

A.4 External and internal mass transfer analysis

A.4.1 Characteristic dimensions for the external and internal mass transfer analysis

In order to study the external and internal mass transfer resistances, two different characteristic cross-sectional areas for a single channel of the monolith are defined: the cross-sectional area of gas phase or circular flow area $A_{\Omega e}$ (m^2) and the cross-sectional area of coated catalyst layer $A_{\Omega i}$ (m^2).

The cross-sectional area of fluid phase $A_{\Omega e}$ (m^2) is calculated as:

$$A_{\Omega e} = \frac{\pi \cdot d_f^2}{4} \quad (S24)$$

where d_f (m) is the average channel dimension estimated by SEM.

The cross-sectional area of coated catalyst layer $A_{\Omega i}$ (m^2) is calculated as:

$$A_{\Omega i} = A_{ch} - A_c \quad (S25)$$

where A_{ch} is the area of a single bare channel (m^2) and A_c is the area remaining available in the channel for the flow of reactants after catalyst deposition (m^2). For the channel shape under consideration (square channel with circular flow area), A_c (m^2) corresponds with the circular flow area $A_{\Omega e}$ (m^2).

The area of a single bare channel A_{ch} (m^2) is calculated as:

$$A_{ch} = l_w^2 \quad (S26)$$

where l_w (m) is the channel width.

Thus, it is possible to define the characteristic length scales for the fluid phase $R_{\Omega e}$ (m) and for the coated catalyst layer $R_{\Omega i}$ (m).

The characteristic length scale for the fluid phase $R_{\Omega e}$ (m) is defined as [47]:

$$R_{\Omega e} = \frac{A_{\Omega e}}{P_c} \quad (\text{S27})$$

where $A_{\Omega e}$ (m²) is the flow area (or cross-sectional area of fluid phase) and P_c (m) is the fluid-coated catalyst layer interfacial perimeter.

The fluid-coated catalyst layer interfacial perimeter is calculated as:

$$P_c = \pi \cdot d_f \quad (\text{S28})$$

Thus, the characteristic length scale for the fluid phase $R_{\Omega e}$ (m) can be expressed as:

$$R_{\Omega e} = \frac{\frac{\pi d_f^2}{4}}{\pi d_f} = \frac{d_f}{4} \quad (\text{S29})$$

The characteristic length scale for the coated catalyst layer $R_{\Omega i}$ (m) is defined as [47]:

$$R_{\Omega i} = \frac{A_{\Omega i}}{P_c} \quad (\text{S30})$$

where $A_{\Omega i}$ (m²) is the cross-sectional area of coated catalyst layer and P_c (m) is the fluid-coated catalyst layer interfacial perimeter.

Thus, the characteristic length scale for the coated catalyst layer $R_{\Omega i}$ (m) can be expressed as:

$$R_{\Omega i} = \frac{l_w^2 \frac{\pi d_f^2}{4}}{\pi d_f} \quad (\text{S31})$$

A.4.2 External and internal mass transfer coefficients

The external mass transfer coefficient $k_{m,e}$ (m s⁻¹) between the bulk of fluid phase and the fluid-coated catalyst layer interface is calculated as [47]:

$$k_{m,e} = \frac{Sh_e \cdot D_{CH_4-mix}}{4 \cdot R_{\Omega e}} \quad (\text{S32})$$

where Sh_e is the external Sherwood number, D_{CH_4-mix} is the diffusivity of CH₄ in gas phase (m² s⁻¹) and $R_{\Omega e}$ is the characteristic length scale for the fluid phase (m).

The internal mass transfer coefficient $k_{m,i}$ (m s⁻¹) between the interior of the coated catalyst layer and fluid-coated catalyst layer interface is calculated as [47]:

$$k_{m,i} = \frac{Sh_i \cdot D_{CH_4,e}}{R_{\Omega i}} \quad (S33)$$

where Sh_i is the internal Sherwood number, $D_{CH_4,e}$ is the effective diffusivity of CH_4 in the coated layer ($m^2 s^{-1}$) and $R_{\Omega i}$ is the characteristic length scale for the coated catalyst (m).

The external Sherwood number Sh_e is calculated by [47]:

$$Sh_e = Sh_{e\infty} + \frac{2.8}{Sc^{1/6}} \cdot \sqrt{P} \quad (S34)$$

where $Sh_{e\infty}$ is the asymptotic external Sherwood number, Sc is the Schmidt (Sc) number and P is the transverse Peclet number. For square channel, $Sh_{e\infty} = 2.98$. The transverse Peclet number is calculated as [47]:

$$P = \frac{R_{\Omega e}^2 \cdot u_o}{L_m \cdot D_{CH_4-mix}} \quad (S35)$$

where $R_{\Omega e}$ is the characteristic length scale for the fluid phase (m), u_o is the inlet gas velocity at operative conditions ($m s^{-1}$), L_m is the monolith length (m) and D_{CH_4-mix} is the diffusivity of CH_4 in gas phase ($m^2 s^{-1}$).

The internal Sherwood number Sh_i is calculated by [47]:

$$Sh_i = Sh_{i\infty} + \frac{\Lambda \cdot \varnothing^2}{1 + \Lambda \cdot \varnothing} \quad (S36)$$

where $Sh_{i\infty}$ is the asymptotic internal Sherwood number, Λ is a constant that depends on the coated catalyst layer shape and kinetic parameters and \varnothing is the Thiele modulus.

The Thiele modulus \varnothing for a first order reaction is defined as:

$$\varnothing = \sqrt{\frac{k_{obs} \cdot R_{\Omega i}^2}{D_{CH_4,e}}} \quad (S37)$$

where k_{obs} is the observed first-order reaction rate constant (s^{-1}), $R_{\Omega i}$ is the effective transverse diffusion length in the coated catalyst layer (m) and $D_{CH_4,e}$ is the effective diffusivity of CH_4 ($m^2 s^{-1}$).

The effectiveness factor η for a first order reaction can be expressed as [47]:

$$\eta = \frac{1}{1 + \frac{\varnothing^2}{Sh_i}} \quad (S38)$$

where \varnothing is the Thiele modulus for a first order reaction and Sh_i is the internal Sherwood number.

A.4.3 Multiple resistances in series approach

The overall resistance for mass transfer R_t ($s\ m^{-1}$) is defined as [47]:

$$R_t = R_e + R_i + R_r \quad (S39)$$

where R_e is the resistance for the external mass transfer ($s\ m^{-1}$), R_i is the resistance for the internal mass transfer ($s\ m^{-1}$) and R_r is the reaction resistance ($s\ m^{-1}$). The resistance for the external mass transfer R_e ($s\ m^{-1}$) can be calculated as:

$$R_e = \frac{1}{k_{m,e}} \quad (S40)$$

where $k_{m,e}$ is the external mass transfer coefficient between the bulk of fluid phase and the fluid-coated catalyst layer interface ($m\ s^{-1}$).

The resistance for the internal mass transfer R_i ($s\ m^{-1}$) can be calculated as:

$$R_i = \frac{1}{k_{m,i}} \quad (S41)$$

where $k_{m,i}$ is the internal mass transfer coefficient between the interior of the coated catalyst layer and fluid-coated catalyst layer interface ($m\ s^{-1}$).

The reaction resistance R_r ($s\ m^{-1}$) can be calculated as:

$$R_t = \frac{1}{k_{obs} \cdot R_{\Omega i}} \quad (S42)$$

where $R_{\Omega i}$ (m) is the characteristic length scale for the coated catalyst layer and k_{obs} (s^{-1}) is the observed first-order reaction rate constant.

Thus, the apparent (or overall experimentally observable) mass transfer coefficient $k_{m,app}$ ($m\ s^{-1}$) can be calculated as [47]:

$$\frac{1}{k_{m,app}} = \frac{1}{k_{m,e}} + \frac{1}{k_{m,i}} + \frac{1}{k_{obs} \cdot R_{\Omega i}} \quad (S43)$$

where $k_{m,e}$ is the external mass transfer coefficient between the bulk of fluid phase and the fluid-coated catalyst layer interface ($m\ s^{-1}$), $k_{m,i}$ is the internal mass transfer coefficient between the interior of the coated catalyst layer and fluid-coated catalyst layer interface ($m\ s^{-1}$), k_{obs} is the observed first-order reaction rate constant (s^{-1}) and $R_{\Omega i}$ is the characteristic length scale for the coated catalyst layer (m).

Writing S.43 in dimensionless form gives:

$$\frac{1}{k_{m,app}} \cdot \frac{D_{CH_4-mix}}{4 \cdot R_{\Omega e}} = \left(\frac{1}{Sh_e} + \frac{R_{\Omega i} \cdot D_{CH_4-mix}}{4 \cdot R_{\Omega e} \cdot D_{CH_4,e} \cdot Sh_i} + \frac{D_{CH_4-mix}}{4 \cdot R_{\Omega e} \cdot k_{obs} \cdot R_{\Omega i}} \right) \quad (S44)$$

$$\frac{1}{Sh_{app}} = \left(\frac{1}{Sh_e} + \frac{\alpha\beta}{4} \cdot \frac{1}{Sh_i} + \frac{\alpha\beta}{4\phi^2} \right) \quad (S45)$$

where the various dimensionless groups appearing in S.45 are defined as:

$$\beta = \frac{R_{\Omega i}}{R_{\Omega e}}, \quad \alpha = \frac{D_{CH_4-mix}}{D_{CH_4,e}}, \quad \phi^2 = \frac{k_{obs} \cdot R_{\Omega i}^2}{D_{CH_4,e}}, \quad Sh_{app} = \frac{4 \cdot k_{m,app} \cdot R_{\Omega e}}{D_{CH_4-mix}} \quad (S46)$$

where $k_{m,app}$ ($m \cdot s^{-1}$) is the apparent (or overall experimentally observable) mass transfer coefficient, $D_{CH_4,e}$ is the effective diffusivity of CH_4 ($m^2 \cdot s^{-1}$), D_{CH_4-mix} is the diffusivity of CH_4 in gas phase mixture ($m^2 \cdot s^{-1}$), $R_{\Omega i}$ is the characteristic length scale for the coated catalyst layer (m), $R_{\Omega e}$ is the characteristic length scale for the fluid phase (m), Sh_i is the internal Sherwood number, Sh_e is the external Sherwood number, k_{obs} is the observed first-order reaction rate constant (s^{-1}), ϕ is the Thiele modulus for a first order reaction and Sh_{app} is the apparent (or experimentally observed) mass transfer coefficient.

In kinetic regime, the apparent mass transfer coefficient can be written as:

$$Sh_{app,kin} = \frac{4 \cdot \phi^2}{\alpha \beta} \quad (S47)$$

A.5 Heat transfer effects

For highly endothermic reactions such as methane steam reforming, temperature gradients between the gas phase and catalyst surface cannot be neglected. Under steady-state conditions, the rate of mass transfer of methane reactant from the gas phase mixture to the solid surface must be equal to the rate of methane reactant conversion by surface reaction:

$$k_{m,e} \cdot A_{\Omega e} \cdot (C_b - C_s) = k_s \cdot A_{\Omega e} \cdot C_s^n \quad (S48)$$

where k_s is the surface reaction rate constant, C_b is the concentration in the bulk of the gas phase ($mol \cdot m^{-3}$), C_s is the concentration in the surface of the catalyst layer ($mol \cdot m^{-3}$).

Assuming that the outer surface of the catalyst particle is uniformly accessible to the reagents, that is, the thickness of the concentration and thermal boundary layers over the particle surface has constant values. Since each section of the outer surface behaves kinetically the same as all other parts, steady-state analysis of such a system is essentially one-dimensional [45, 59]. Thus, the heat generated by the surface reaction can be calculated by multiplying the mass transfer rate with the heat of reaction per mol of reactant. At steady state, we can obtain:

$$k_{m,e} \cdot A_{\Omega e} \cdot (C_b - C_s) \cdot (\Delta H_r) = h_e \cdot A_{\Omega e} \cdot (T_b - T_s) \quad (S49)$$

Solving the temperature difference, the final expression is given by:

$$\frac{k_{m,e}}{h_e} \cdot (C_b - C_s) \cdot (\Delta H_r) = (T_b - T_s) \quad (\text{S50})$$

where T_b, T_s is the temperature in the bulk of the gas phase and surface of the catalyst layer (K) respectively, ΔH_r is the heat of MSR reaction (J mol^{-1}) and h_e is the heat transfer coefficient associated for the gas phase ($\text{W m}^{-2} \text{K}^{-1}$).

Hence, using the Chilton–Colburn analogy between heat and mass transfer ($j_H \approx j_M$) for simple gas mixture, we can replace the ratio $\frac{k_{m,e}}{h_e}$ and obtain the following expression [45, 59]:

$$k_{m,e} = \frac{j_M \cdot G}{\rho_f \cdot Sc^{\frac{2}{3}}} \quad h_e = \frac{j_H \cdot G \cdot Cp_f}{Pr^{\frac{2}{3}}} \quad (\text{S51})$$

$$(T_b - T_s) = \frac{\Delta H_r}{\rho_f \cdot Cp_f} \cdot \left(\frac{Pr}{Sc}\right)^{\frac{2}{3}} \cdot (C_b - C_s) \quad (\text{S52})$$

Considering the Lewis (Le) and Carberry (Ca) number, we can obtain the final expression as [45, 59]:

$$Le = \frac{Sc}{Pr} \quad Ca = \frac{C_b - C_s}{C_b} \quad (\text{S53})$$

$$(T_b - T_s) = \left(\frac{\Delta H_r \cdot C_b}{\rho_f \cdot Cp_f}\right) \cdot Le^{-2/3} \cdot Ca \quad (\text{S54})$$

where ρ_f is the density of the gas phase (Kg m^{-3}), $c_{p,f}$ is the heat capacity of the gas phase ($\text{J Kg}^{-1} \text{K}^{-1}$) and Pr is the Prandtl number.

Thus, by dividing Eq. S.53 by T_b , it is possible to obtain the dimensionless external Prater number (β_{ext}) which represents the ratio of the maximum heat consumption and heat transfer rates:

$$\frac{T_s}{T_b} = 1 - \left(\frac{\Delta H_r \cdot C_b}{\rho_f \cdot Cp_f}\right) \cdot \frac{1}{T_b} \cdot Le^{-2/3} \cdot Ca \quad (\text{S55})$$

$$\frac{T_s}{T_b} = 1 - \frac{\Delta T_{ad}}{T_b} \cdot Le^{-2/3} \cdot Ca \quad (\text{S56})$$

$$\frac{T_s}{T_b} = 1 - \beta_{ext} \cdot Ca \quad (\text{S57})$$

where ΔT_{ad} is the adiabatic temperature rise ($\Delta T_{ad} = \frac{\Delta H_r \cdot C_b}{\rho_f \cdot Cp_f}$; K) and β_{ext} is the dimensionless external Prater number ($\beta_{ext} = \frac{\Delta T_{ad}}{T_b} \cdot Le^{-2/3}$).

The interphase heat transfer limitations can be evaluated using the criterion derived by Mears [61] (Eq. S.58) with the perturbation approach, in which the heat transfer resistance of the fluid phase is assumed to be lumped at the surface:

$$\chi = \frac{(\Delta H \cdot R^{obs} \cdot R_{\Omega e})}{h_e \cdot T_b} < \frac{0.15}{\gamma_b}; \quad \gamma_b = \frac{E_{act}}{R_g \cdot T_b} \quad (S58)$$

where R^{obs} is the observed reaction rate ($\text{mol m}^3 \text{s}^{-1}$), h_e is the heat transfer coefficient associated for the gas phase ($\text{W m}^{-2} \text{K}^{-1}$), R_g is the gas constant ($\text{J mol}^{-1} \text{K}^{-1}$), E_{act} is the apparent activation energy of the reaction (J mol^{-1}), χ is the Damkohler for interphase heat transport and γ_b is the Arrhenius number evaluated at the bulk of the gas phase.

Anderson in 1963 [62] applied the perturbation approach to derive a criterion for the lack of importance of temperature gradients in catalyst particles. The reaction is assumed to follow Arrhenius temperature dependence and this criterion is valid regardless of whether there are diffusion limitations in the particle or not:

$$\frac{(\Delta H \cdot R^{obs} \cdot R_{\Omega i}^2)}{\lambda_{cat} \cdot T_s} < \frac{0.75}{\gamma_s} \quad (S59)$$

$$\psi = \frac{(\Delta H \cdot R^{obs} \cdot R_{\Omega i}^2)}{\lambda_{cat} \cdot T_s}; \quad \gamma_s = \frac{E_{act}}{R_g \cdot T_s} \quad (S60)$$

where λ_{cat} is the thermal conductivity of the Ru/Al₂O₃ catalyst ($\text{W m}^{-1} \text{K}^{-1}$), ψ is the Damkohler for intraparticle heat transport and γ_s is the Arrhenius number evaluated at the surface of the gas phase.

In order to study the effects of mass and heat transfer, both balances must be solved simultaneously to estimate the concentration and temperature profile. From the mass balance, we can write the following expression:

$$D_e \cdot \frac{d^2 c}{dx^2} - (-R) = 0 \quad (S61)$$

The heat balance can be written as:

$$\lambda_e \frac{d^2 T}{dx^2} - (-R) \cdot (\Delta H_r) = 0 \quad (S62)$$

where λ_e is the effective thermal conductivity ($\text{W m}^{-1} \text{K}^{-1}$). Considering that the reaction rate (R) is the same in both balances, we can obtain the following expression:

$$\frac{D_e \cdot (\Delta H_r)}{\lambda_e} \cdot \frac{d^2 c}{dx^2} = \frac{d^2 T}{dx^2} \quad (S63)$$

By integrating the Equation S.63 and considering the surface concentration and temperature (C_s, T_s), we can obtain the following linear expression between internal temperature and reactant concentration [15,16]:

$$(T_s - T_{b,c}) = (\Delta H_r) \cdot \frac{D_e}{\lambda_e} \cdot (C_s - C_{b,c}) \quad (\text{S64})$$

where $T_{b,c}$ is the temperature in the bulk of the catalyst layer (K) and $C_{b,c}$ is the concentration within the catalyst layer (mol m^{-3}). It is worth noting the largest possible temperature difference into the catalyst layer is attained when the concentrations within the bulk of the catalyst layer becomes zero, hence we can refer the maximum temperature difference (ΔT_{max}) to the surface temperature using the dimensionless internal Prater number (β_{in}) by [15,16]:

$$\beta_{in} = \frac{\Delta T_{max}}{T_s} = \frac{(\Delta H_r) \cdot C_s}{T_s} \cdot \frac{D_e}{\lambda_e} \quad (\text{S65})$$

Σ	[cpsi]	100
D_m	[m]	0.030
L_m	[m]	0.0019
δ_w	[m]	0.00063
N	[m]	0.1563
E	[-]	0.564
GSA	[$\text{m}^2 \text{m}^{-3}$]	1187,333
d_h	[m]	0.0019
A_m	[m]	0.00126

Table A5. Properties of the bare monolith.

T [°C]	t_c [s]	t_d^i [s]	t_d^e [s]	t_r [s]	t_z [s]
550	0.3091	0.0456	0.0012	0.2238	5.1500
600	0.2914	0.0441	0.0010	0.1928	4.5926
650	0.2756	0.0428	0.0009	0.1883	4.1264
700	0.2615	0.0405	0.0008	0.1441	3.6903
750	0.2487	0.0394	0.0007	0.1151	3.3138
800	0.2371	0.0384	0.0007	0.0943	2.9217
850	0.2266	0.0384	0.0006	0.0939	2.6402

Table A6. Characteristic times for the 1.5Ru5Al catalyst.

T [°C]	t_c [s]	t_d^i [s]	t_d^e [s]	t_r [s]	t_z [s]
550	0.3091	0.0714	0.0010	0.1521	4.5226
600	0.2914	0.0691	0.0008	0.1212	3.9330
650	0.2756	0.0670	0.0007	0.1113	3.4816
700	0.2614	0.0651	0.0007	0.1040	3.1674
750	0.2487	0.0634	0.0006	0.1001	2.9079
800	0.2371	0.0618	0.0006	0.1001	2.6688
850	0.2266	0.0604	0.0005	0.1014	2.4751

Table A7. Characteristic times for the 1.5Ru10Al catalyst.

T [°C]	t_c [s]	t_d^i [s]	t_d^e [s]	t_r [s]	t_z [s]
550	0.3091	0.1319	0.0008	0.4222	4.7509
600	0.2914	0.1277	0.0008	0.3860	4.2279
650	0.2756	0.1239	0.0007	0.3713	3.8065
700	0.2614	0.1204	0.0006	0.3459	3.4299
750	0.2487	0.1172	0.0006	0.3495	3.1437
800	0.2371	0.1142	0.0005	0.3401	2.8716
850	0.2266	0.1115	0.0005	0.3195	2.6049

Table A8. Characteristic times for the 1.5Ru20Al catalyst.

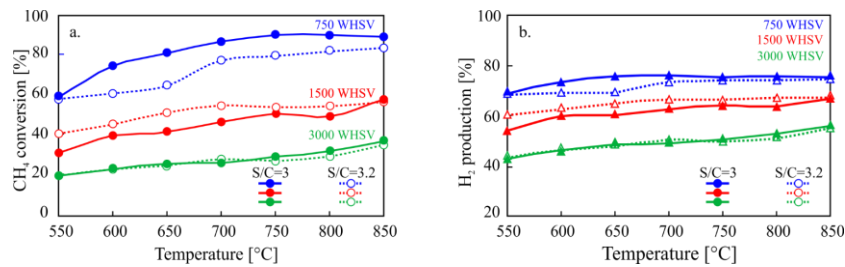


Fig. A1. MSR tests, performance comparison of monoliths 1.5% Ru on 10% γ - Al_2O_3 at various WHSV and S/C a) CH_4 conversion; b) H_2 production.

6. REFERENCES

- [1] Hosseini, S.E., Wahid, M.A. Hydrogen production from renewable and sustainable energy resources: Promising green energy carrier for clean development. *Renew. Sustain. Energy Rev.* 57 (2016)850–866.

- [2] IAEA (1999) IAEA-TECDOC-1085: Hydrogen as an energy carrier and its production by nuclear power. Iaea-Tecd-1085
- [3] Alves, J.J., Towler, G.P. Analysis of refinery hydrogen distribution systems. *Ind. Eng. Chem. Res.* 41 (2002) 5759–5769.
- [4] Meyers, R.A. *Handbook of petroleum Refining Processes*, Second. McGraw-Hill, New York (1996).
- [5] Yamaguchi, D., Tang, L., Burke, N., et al. Small Scale Hydrogen Production from Metal-Metal Oxide Redox Cycles. *Hydrog Energy - Challenges Perspect.* 2 (2012) 31–54.
- [6] Karadag, D., K ro lu, O.E., Ozkaya, B., et al. A review on fermentative hydrogen production from dairy industry wastewater. *J. Chem. Technol. Biotechnol.* 89 (2014) 1627–1636.
- [7] Holladay, J.D., Hu, J., King, D.L., Wang, Y. An overview of hydrogen production technologies. *Catal. Today* 139 (2009) 244–260.
- [8] Barreto, L., Makihiro, A., Riahi, K. The hydrogen economy in the 21st century: A sustainable development scenario. *Int. J. Hydrogen Energy* 28 (2003) 267–284.
- [9] Hansen, K., Ingerslev, M., Felby, C., et al. Bioenergy in the Nordic-baltic-NW Russian Region. 66 (2006).
- [10] Abbas, S.Z., Dupont, V., Mahmud, T. Kinetics study and modelling of steam methane reforming process over a NiO/Al₂O₃ catalyst in an adiabatic packed bed reactor. *Int. J. Hydrogen Energy* 42 (2017) 2889–2903.
- [11] De, S., Zhan, J., Luque, R., Yan, N. Ni-based bimetallic heterogeneous catalysts for energy and environmental applications. *Energy Environ. Sci.* 9 (2016) 3314–3347.
- [12] Omoregbe, O., Danh, H.T., Abidin, S.Z., et al. Influence of Lanthanide Promoters on Ni/SBA-15 Catalysts for Syngas Production by Methane Dry Reforming. *Procedia Eng.* 148 (2016) 1388–1395.
- [13] Tsyganok, A.I., Inaba, M., Tsunoda, T., et al. Dry reforming of methane over supported noble metals: A novel approach to preparing catalysts. *Catal Commun* 4 (2003) 493–498.
- [14] Rass-Hansen, J., Christensen, C.H., Sehested, J., et al. Renewable hydrogen: Carbon formation on Ni and Ru catalysts during ethanol steam-reforming. *Green Chem.* 9 (2007) 1016–1021.
- [15] Rostrup-Nielsen, J.R., Bak Hansen, J.H. CO₂-reforming of methane over transition metals. *J. Catal.* 144 (1993) 38–49.
- [16] Ashraf, M.A., Sanz, O., Italiano, C., et al. Analysis of Ru/La-Al₂O₃ catalyst loading on alumina monoliths and controlling regimes in methane steam reforming. *Chem. Eng. J.* 334 (2018) 1792–1807.
- [17] Tjiburg, I.I.M., Geus, J.W., Zandbergen, H.W. Application of lanthanum to pseudo-boehmite and γ -Al₂O₃. *J. Mater. Sci.* 26 (1991) 6479–6486.
- [18] Arai, H., Machida, M. Thermal stabilization of catalyst supports and their application to high-temperature catalytic combustion. *Appl. Catal. A Gen.* 138 (1996) 161–176
- [19] Ferreira-Aparicio, P., Rodr guez-Ramos, I., Anderson, J.A., Guerrero-Ruiz, A. Mechanistic aspects of the dry reforming of methane over ruthenium

- catalysts. *Appl. Catal. A Gen.* 202 (2000) 183–196.
- [20] Berman, A., Karn, R.K., Epstein, M. Steam reforming of methane on a Ru/Al₂O₃ catalyst promoted with Mn oxides for solar hydrogen production. *Green Chem.* 9 (2007) 626–631.
 - [21] Amjad, U., Vita, A., Galletti, C., et al. Comparative study on steam and oxidative steam reforming of methane with noble metal catalysts. *Ind. Eng. Chem. Res.* 52 (2013) 15428–15436.
 - [22] Amjad, U., Moncada Quintero, C.W., Ercolino, G., et al. Methane Steam Reforming on the Pt/CeO₂ Catalyst: Effect of Daily Start-Up and Shut-Down on Long-Term Stability of the Catalyst. *Ind. Eng. Chem. Res.* 58 (2019) 16395–16406.
 - [23] Italiano, C., Ashraf, M.A., Pino, L., et al. Rh/CeO₂ thin catalytic layer deposition on alumina foams: Catalytic performance and controlling regimes in biogas reforming processes. *Catalysts* 8 (2018) 1–25.
 - [24] Vita, A., Italiano, C., Ashraf, M.A., et al. Syngas production by steam and oxy-steam reforming of biogas on monolith-supported CeO₂-based catalysts. *Int. J. Hydrogen Energy* 43 (2018) 11731–11744.
 - [25] Govender, S., Friedrich, H.B. Monoliths: A review of the basics, preparation methods and their relevance to oxidation. *Catalysts* 7 (2017).
 - [26] Roy, S., Bauer, T., Al-Dahhan, M., et al. Monoliths as multiphase reactors: A review. *AIChE J.* 50 (2004) 2918–2938.
 - [27] Boger, T., Heibel, A.K., Sorensen, C.M. Monolithic catalysts for the chemical industry. *Ind. Eng. Chem. Res.* 43 (2004) 4602–4611.
 - [28] Visconti, C.G., Tronconi, E., Groppi, G., et al. Monolithic catalysts with high thermal conductivity for the Fischer-Tropsch synthesis in tubular reactors. *Chem. Eng. J.* 171 (2011) 1294–1307.
 - [29] Tronconi, E., Groppi, G., Visconti, C.G. Structured catalysts for non-adiabatic applications. *Curr. Opin. Chem. Eng.* 5 (2014) 55–67.
 - [30] Ercolino, G., Karimi, S., Stelmachowski, P., Specchia, S. Catalytic combustion of residual methane on alumina monoliths and open cell foams coated with Pd/Co₃O₄. *Chem. Eng. J.* 326 (2017) 339–349.
 - [31] Ercolino, G., Stelmachowski, P., Specchia, S. Catalytic Performance of Pd/Co₃O₄ on SiC and ZrO₂ Open Cell Foams for Process Intensification of Methane Combustion in Lean Conditions. *Ind. Eng. Chem. Res.* 56 (2017) 6625–6636.
 - [32] Ercolino, G., Grzybek, G., Stelmachowski, P., et al. Pd/Co₃O₄-based catalysts prepared by solution combustion synthesis for residual methane oxidation in lean conditions. *Catal. Today* 257 (2015) 66–71.
 - [33] Vita, A., Cristiano, G., Italiano, C., et al. Methane oxy-steam reforming reaction: Performances of Ru/ γ -Al₂O₃ catalysts loaded on structured cordierite monoliths. *Int. J. Hydrogen Energy* 39 (2014) 18592–18603.
 - [34] Specchia, S., Galletti, C., Specchia, V. Solution Combustion Synthesis as intriguing technique to quickly produce performing catalysts for specific applications. *Stud. Surf. Sci. Catal.* 175 (2010) 59–67.
 - [35] Nijhuis, T.A., Beers, A.E.W., Vergunst, T., et al. Preparation of monolithic catalysts. *Catal. Rev. - Sci. Eng.* 43 (2001) 345–380.

- [36] Williams, J.L. Monolith Structures, Materials, Properties and Uses. *Catal. Today* 69 (2001) 3–9.
- [37] Plummer, H.K., Baird, R.J., Hammerle, R.H., et al. Measurement of automotive catalyst washcoat loading parameters by microscopy techniques. *Microsc. Microanal.* 5 (1999) 267–281.
- [38] Cybulski, A., Moulijn, J.A. *Structured Catalysts and Reactors*. Marcel Dekker, Inc., New York (1998).
- [39] Wójcik, S., Ercolino, G., Gajewska, M., et al. Robust $\text{Co}_3\text{O}_4|\alpha\text{-Al}_2\text{O}_3$ |cordierite structured catalyst for N_2O abatement – Validation of the SCS method for active phase synthesis and deposition. *Chem. Eng. J.* (2018) in press.
- [40] Millington, B., Whipple, V., Pollet, B.G. A novel method for preparing proton exchange membrane fuel cell electrodes by the ultrasonic-spray technique. *J. Power Sources* 196 (2011) 8500–8508.
- [41] Arzamendi, G., Die, P.M., Gandia, L.M. *Renewable hydrogen technologies: Renewable hydrogenenergy - An overview* (2013).
- [42] Spivey, J.J., Dooley, K.M. *Catalysis*. The Royal Society of Chemistry (2009).
- [43] Dumesic, J.A., Huber, G.W., Boudart, M. *Principles of Heterogeneous Catalysis*. In: *Handbook of Heterogeneous Catalysis*. Wiley-VCH Verlag GmbH & Co. KGaA (2008).
- [44] Klaewkla, R., Arend, M., Hoelderich, W.F. A Review of Mass Transfer Controlling the Reaction Rate in Heterogeneous Catalytic Systems. In: *Mass Transfer - Advanced Aspects*. pp 667–684 (2011).
- [45] Kashid, M.N., Renken, A. *Microstructured Devices for Chemical Microreactors*. Wiley-VCH Verlag GmbH & Co. (2013)
- [46] Joshi, S.Y., Harold, M.P., Balakotaiah, V. Low-Dimensional Models for Real Time Simulations of Catalytic Monoliths. *AIChE J.* 55 (2009) 1771–1783.
- [47] Joshi, S.Y., Harold, M.P., Balakotaiah, V. Overall mass transfer coefficients and controlling regimes in catalytic monoliths. *Chem. Eng. Sci.* 65 (2010) 1729–1747.
- [48] Joshi, S.Y., Harold, M.P., Balakotaiah, V. On the use of internal mass transfer coefficients in modeling of diffusion and reaction in catalytic monoliths. *Chem. Eng. Sci.* 64 (2009) 4976–4991.
- [49] Balakotaiah, V., West, D.H. Shape normalization and analysis of the mass transfer controlled regime in catalytic monoliths. *Chem. Eng. Sci.* 57 (2002) 1269–1286.
- [50] Young, L.C., Finlayson, B.A. Mathematical models of the monolith catalytic converter: Part II. Application to automobile exhaust. *AIChE J.* 22 (1976) 343–353.
- [51] Bhattacharya, M., Harold, M.P., Balakotaiah, V. Mass-transfer coefficients in washcoated monoliths. *AIChE J.* 50 (2004) 2939–2955.
- [52] Balakotaiah, V. On the relationship between Aris and Sherwood numbers and friction and effectiveness factors. *Chem. Eng. Sci.* 63 (2008) 5802–5812.

- [53] Laguna, O.H., Domínguez, M.I., Centeno, M.A., Odriozola, J.A. Catalysts on Metallic Surfaces: Monoliths and Microreactors. New Materials for Catalytic Applications. Elsevier B.V. (2016).
- [54] Kockmann, N. Transport Phenomena in Micro Process Engineering. Norbert Kockmann, Springer (2008).
- [55] Bennett, C.J., Hayes, R.E., Kolaczowski, S.T., Thomas, W.J. An experimental and theoretical study of a catalytic monolith to control automobile exhaust emissions. *Proc. R. Soc. Lond. A* 439 (1992) 465–483.
- [56] Joshi, S.Y., Ren, Y., Harold, M.P., Balakotaiah, V. Determination of kinetics and controlling regimes for H₂ oxidation on Pt/Al₂O₃ monolithic catalyst using high space velocity experiments. *Appl. Catal. B Environ.* 102 (2011) 484–495.
- [57] Berman, A., Karn, R.K., Epstein, M. Kinetics of steam reforming of methane on Ru/Al₂O₃ catalyst promoted with Mn oxides. *Appl. Catal. A Gen.* 282 (2005) 73–83.
- [58] Choudhary, T.V., Goodman, D.W. Methane activation on Ni and Ru model catalysts. *J. Mol. Catal. A Chem.* 163 (2000) 9–18.
- [59] Onsan, Z.I., Avci, A.K. Multiphase Catalytic Reactors. John Wiley & Sons, Hoboken, N.J. (2016).
- [60] Shah, R.K., London, A.L. Laminar Flow Forced Convection in Ducts: A Source Book for Compact Heat Exchanger Analytical Data. Academic Press, New York (1978)
- [61] Mears, D.E. Diagnostic criteria for heat transport limitations in fixed bed reactors. *J. Catal* 20 (1971) 127–131.
- [62] Anderson, J.E. A criterion for isothermal behaviour of a catalyst pellet. *Chem. Eng. Sci.* 18 (1963) 147–148.
- [63] Damköhler, G. The Excess Temperature in Contact Grains. *Z Phys Chemie* 193 (1943) 16–28.
- [64] Yaws, .CL. Chemical properties Handbook. McGraw-Hill, New York (1999).
- [65] Fuller, E.N., Schettler, P.D., Giddings, J.C. A new method for prediction of binary gas-phase diffusion coefficients. *Ind. Eng. Chem.* 58 (1966) 18–27.
- [66] Green, D.W., Perry, R.H. Perry's Chemical Engineers' Handbook, 8th ed. McGraw-Hill (2008).
- [67] Cao, C., Zhang, N., Cheng, Y. Numerical analysis on steam methane reforming in a plate microchannel reactor: Effect of washcoat properties. *Int. J. Hydrogen Energy* 41 (2016) 18921–18941.
- [68] Hayes, R.E., Kolaczowski, S.T., Li, P.K.C., Awdry, S. Evaluating the effective diffusivity of methane in the washcoat of a honeycomb monolith. *Appl. Catal. B Environ.* 25 (2000) 93–104.
- [69] Talebian-Kiakalaieh, A., Amin, N.A.S. Theoretical and experimental evaluation of mass transfer limitation in gas phase dehydration of glycerol to acrolein over supported HSiW catalyst. *J. Taiwan Inst. Chem. Eng.* 59 (2016) 11–17.
- [70] Kolitcheff, S., Jolimaître, E., Hugon, A., et al. Tortuosity of mesoporous alumina catalyst supports: Influence of the pore network organization.

- Microporous Mesoporous Mater 248 (2017) 91–98.
- [71] Satterfield, C.N. Mass Transfer in Heterogeneous Catalysis. Massachusetts Institute of Technology Press, Cambridge (1970).
- [72] Ertl, G., Knözinger, H., Weitkamp, J. Handbook of heterogeneous catalysis. VCH, Weinheim (1997).
- [73] Incera Garrido, G., Patcas, F.C., Lang, S., Kraushaar-Czarnetzki, B. Mass transfer and pressure drop in ceramic foams: A description for different pore sizes and porosities. Chem. Eng. Sci. 63 (2008) 5202–5217.